Directed evolution-based discovery of ligands for in vivo restimulation of CAR-T cells

Authors: Leyuan Ma[1,7,8,10,13]*, Ranjani Ramasubramanian[12,13], Naveen K. Mehta[1], Benjamin Cossette[1], Duncan M. Morgan[1,4], Ina Sukaj[1], Elisa Bergaggio[15], Stephan Kadauke[7], Regina M. Myers[11,14], Luca Paruzzo[8,9,10], Guido Ghilardi[8,9,10], Tomasz M. Grzywa[13], Austin Cozzone[13], Stephen J. Schuster[9,10], Noelle Frey[9,10], Libin Zhang[1], Parisa Yousefpour[1], Wuhbet Abraham[1], Heikyung Suh[1], Marco Ruella[8,9,10], Stephan A. Grupp[7,11,14], Roberto Chiarle[15,16], K. Dane Wittrup[1,3,4], Darrell J. Irvine[1,2,3,5,6]*

Affiliations:

[1]David H. Koch Institute for Integrative Cancer Research, MIT, Cambridge, MA, 02139, USA.
[2]Department of Materials Science and Engineering, MIT, Cambridge, MA, 02139, USA.
[3]Department of Biological Engineering, MIT, Cambridge, MA, 02139, USA.
[4]Department of Chemical Engineering, MIT, Cambridge, MA, USA.
[5]Ragon Institute of Massachusetts General Hospital, Cambridge, MA, 02139, USA.
[6]Howard Hughes Medical Institute, Chevy Chase, MD, 20815, USA.
[7]Department of Pathology and Laboratory Medicine, Perelman School of Medicine, University of Pennsylvania, Philadelphia, PA 19104, USA.
[8]Center for Cellular Immunotherapies, University of Pennsylvania, Philadelphia, PA 19104, USA
[9]Division of Hematology/Oncology, University of Pennsylvania Perelman School of Medicine, Philadelphia, PA 19104, USA
[10]Abramson Cancer Center, University of Pennsylvania, Philadelphia, PA 19104, USA
[11]Division of Oncology, Department of Pediatrics, Perelman School of Medicine, University of Pennsylvania, Philadelphia, PA
[12]Department of Bioengineering, School of Engineering and Applied Science, University of Pennsylvania, Philadelphia, PA 19104, USA
[13]The Raymond G. Perelman Center for Cellular and Molecular Therapeutics, Children's Hospital of Philadelphia, Philadelphia, PA 19104, USA
[14]Cellular Therapy and Transplant Section and Cancer Immunotherapy Program, Children's Hospital of Philadelphia, Philadelphia, PA 19104, USA
[15]Department of Pathology, Boston Children's Hospital and Harvard Medical School, Boston, MA 02115, USA
[16]Department of Molecular Biotechnology and Health Sciences, University of Torino, 10126 Torino, Italy

* Correspondence: Leyuan.ma@pennmedicine.upenn.edu (L.M.), djirvine@mit.edu (D.J.I)

Abstract

Chimeric antigen receptor (CAR) T cell therapy targeting CD19 elicits remarkable clinical efficacy in B-cell malignancies, but many patients relapse due to failed expansion and/or progressive loss of CAR-T cells. We recently reported a strategy to potently restimulate CAR-T cells *in vivo*, enhancing their functionality by administration of a vaccine-like stimulus comprised of surrogate peptide ligands for a CAR linked to a lymph node-targeting amphiphilic PEG-lipid (termed CAR-T-vax). Here, we demonstrate a general strategy to generate and optimize peptide mimotopes enabling CAR-T-vax generation for any CAR. Using the clinical CD19 CAR FMC63 as a test case, we employed yeast surface display to identify peptide binders to soluble IgG versions of FMC63, which were subsequently affinity matured by directed evolution. CAR-T vaccines using these optimized mimotopes triggered marked expansion of both murine CD19 CAR-T cells in a syngeneic model and human CAR-T cells in a humanized mouse model of B cell acute lymphoblastic leukemia (B-ALL), and enhanced control of leukemia progression. This approach thus enables vaccine boosting to be applied to any clinically-relevant CAR-T cell product.

Introduction

CD19-targeted chimeric antigen receptor (CAR) T cell therapy elicits impressive anti-tumor activity in the treatment of relapsed or refractory B-cell acute lymphoblastic leukemia (B-ALL) and lymphoma in both pediatric and adult patients[1,2]. This clinical success led to the FDA approval of four CD19-targeted CAR-T products, namely TECARTUS, KYMRIAH, YESCARTA, and BREYANZI[1]. However, a significant fraction (30-60%) of patients still experience leukemia relapse, among which ~50% are CD19-positive relapses[3], suggesting impaired function and/or persistence of the infused CAR-T cells. Robust CAR-T cell engraftment and expansion *in vivo* is a prerequisite for antitumor efficacy[4], a feature that is affected by several characteristics of the CAR-T cell product such as T cell quality[5], CAR designs[3,4,6] and the proportion of early memory T cells in the product[7]. In current CAR-T cell therapy treatment regimens, patients usually receive lymphodepletion to promote CAR-T cell engraftment[8]. Interestingly, multiple reports have shown a correlation between the early-stage expansion of CAR-T cells and initial tumor burden[8,9]. These findings suggest the capacity of CAR-T cells to receive antigen-specific stimulation post infusion is critical for CAR-T cell expansion, engraftment, and potentially long-term persistence. However, whether the antigens presented by tumor cells are sufficient to optimally stimulate CAR-T cells remains unclear.

Vaccination is a natural process whereby T-cells receive antigen-specific stimulation leading to proliferation, differentiation, and induction of effector functions[10]– effects which could be beneficial in promoting CAR-T cell function *in vivo*. However, traditional vaccines provide antigen that must be processed into peptides by professional antigen presenting cells (APCs) and presented on MHC molecules to stimulate T-cells through the T-cell receptor (TCR). This is challenging to adapt to the setting of engineered CAR-T cells, as current CAR-T products are polyclonal and express uncharacterized TCRs. Further, recent next-generation engineering efforts such as knocking CARs into the TCR locus produce CAR-T lacking endogenous TCRs[11]. Proof of concept demonstration of CAR-T cells generated from virus-specific T cells followed by vaccine boosting via the viral-specific TCR has been shown in small clinical trials, yet the benefits observed with this approach have been limited[12,13].

To overcome these issues, we recently developed a molecularly-targeted amphiphilic vaccine (amph-vax) approach to directly stimulate CAR-T cells through the chimeric antigen receptor[14,15]. Amph-vax molecules were generated by linking a CAR-ligand to albumin-binding phospholipid polymers. Following parenteral injection, these CAR-ligand conjugates associate with endogenous albumin present in interstitial fluid and are carried into lymph and downstream draining lymph nodes (dLNs). In the dLN, the lipid tails of amph-vax ligands insert into cell membranes, including membranes of professional APCs, allowing APCs to directly “present” the CAR ligand to CAR-T cells together with additional co-stimulation and cytokine support, making them *de novo* CAR-T cell-priming APCs (**Extended Data Fig. 1**)[14]. Amph-vax stimulation led to pronounced CAR-T cell expansion with enhanced functionality, memory formation and substantially enhanced tumor clearance[14,15]. Importantly, we also found that vaccine boosting of CAR-T cells promotes antigen spreading and the induction of endogenous anti-tumor immune responses, which prevent antigen loss-mediated tumor escape[15]. We demonstrated these effects using CARs that recognize synthetic ligands (e.g., fluorescein) and a model EGFRvIII-specific CAR, where the scFv domain of the chimeric receptor recognizes a linear peptide epitope in EGFRvIII that is readily synthesized as an amph-ligand. However, to generalize this strategy and enable amph-vax boosting with any arbitrary CAR of interest, an approach is needed for *de novo* generation of surrogate peptide ligands for chimeric antigen receptors.

Here, we demonstrate a workflow to identify peptide mimotope ligands for CAR receptors using yeast surface display-based directed evolution[16], which allows for the generation of amph-vaccines that can be used with any CAR system. We demonstrate the pipeline by discovering an amph-ligand that can be used with all four FDA-approved CD19 CAR-T cell therapies. We created

a customized mimotope yeast library to identify peptides that bind to the licensed CD19 CARs. Affinity maturation of hits from this library led to identification of a peptide with high affinity for the CAR. An amphiphile mimotope (amph-mimotope) vaccine based on this peptide efficiently stimulated CD19 CAR-T cells *in vitro*, triggered their expansion *in vivo*, and enhanced clearance of tumors in humanized mouse models of leukemia. To show generality, we also generated amph-mimotopes for a second human CAR recognizing the anaplastic lymphoma kinase (ALK) antigen and a murine CD19 CAR. Collectively, these results show the successful development of a clinically translatable amph-mimotope vaccine with the potential endowing currently FDA-approved CD19 CAR-T cell therapies with enhanced anti-leukemic activity.

Results

Antigen$^+$ tumor cells drive transient CD19 CAR-T expansion but are insufficient to promote long-term CAR-T persistence

CD19 positive relapse is often associated with limited CAR-T persistence and/or impaired functionality[3,17]. To provide insight into whether the level of available antigen stimulation impacts early CAR-T expansion/persistence, we analyzed data from several early clinical trials in children and young adults (CAYA) with B-ALL from the Children's Hospital of Philadelphia (NCT01626495 [18] and NCT02906371[19]) and in adult patients with B-ALL (NCT02030847[20]) or B-cell lymphoma (NCT02030834[21]) from the University of Pennsylvania. We found that CAR-T cell expansion is generally associated with initial tumor burden, with CAR-T cells infused into patients with high tumor burden (>40% bone marrow blasts in pre-infusion bone marrow aspirate) exhibiting more pronounced expansion and longer persistence (**Fig. 1A-C, Extended Data Fig. 2A-B**). This association is statistically significant in CAYA with B-ALL (**Fig. 1A-C**) and exhibits a trend towards significance in adult B-ALL and B-cell lymphoma (**Extended Data Fig. 2A-B**), consistent with observations from earlier studies[8,9].

Since CD19 CAR-T cells target normal B cells, continued B cell aplasia can be used as a pharmacodynamic measure for the presence of functional CD19 CAR-T cells[22]. Nearly half of the pediatric B-ALL patients receiving CD19 CAR-T cell therapy experienced B cell recovery after initial B cell aplasia (**Fig. 1D**), indicating loss of functional CAR-T cells. Interestingly, there was no significant association between the initial tumor burden and the probability of B cell recovery, suggesting that increased early stimulation from tumor cells was not sufficient to maintain CAR-T function. A recent long-term follow-up study found that a higher ratio of peak CAR-T expansion to tumor burden correlates with overall survival and is a better prediction of long-term survival than the absolute magnitude of T cell expansion or tumor burden[23]. These data suggest that if CAR-T cells receive greater antigen stimulation following infusion, they can undergo greater expansion, an important correlate of response to therapy[23,24]. However, sustained anti-tumor function over time requires that T-cells receive restimulation by professional APCs, particularly dendritic cells (DCs), which express high levels of costimulatory receptors and cytokines that are lacking on tumor cells and resting B cells[25,26]. By mining a published dataset[27], we observed significantly higher co-stimulatory molecule expression in DCs than healthy and likely-malignant B cells in B-ALL patients (**Fig. 1E, Extended Data Fig. 3A-H**). We previously also observed that the comprehensive suite of costimulatory molecules expressed by DCs is essential for promoting memory differentiation and optimal amplification of CAR-T cells[14]. These observations suggested to us that an efficient and safe DC-targeted vaccination approach to reinvigorate and sustain CAR-T cell function could be impactful for enhancing current clinical CD19-targeting CAR-T cell therapies.

Discovery of peptide ligands for CARs using yeast surface display

203 We previously demonstrated that a CAR-specific amph-vaccine could provide potent stimulation
204 of CAR-T cells *in vivo*[14,15]. The vaccine was created by linking a CAR ligand to an albumin-binding
205 PEG-lipid, which upon co-administration with adjuvant, would efficiently traffic to draining lymph
206 nodes and decorate the surface of APCs, allowing presentation of the ligand to CAR-T cells in
207 the LN (**Extended Data Fig. 1**). We demonstrated this proof of concept using CARs that
208 recognized arbitrary small molecule ligands (e.g., fluorescein) or linear peptide epitopes. However,
209 the antibody-based antigen-binding domain of the FDA-approved CD19 CARs (which employ an
210 antibody clone known as FMC63) bind to a conformational epitope spanning multiple domains of
211 the human CD19 antigen[28]. Further, the CD19 extracellular domain (ECD) is difficult to express
212 and prone to misfolding[29], making it challenging to use recombinant CD19 for manufacturing an
213 amphiphile vaccine to stimulate CD19 CAR-T cells. As it is common for CAR binding domains to
214 recognized complex conformational epitopes[30–32], we sought to establish a general strategy to
215 generate simple surrogate ligands for any CAR. We hypothesized that generation of mimotopes,
216 linear synthetic peptides that are also recognized by the CAR binding domain in addition to its
217 native target antigen, could be an ideal option (**Fig. 2A**).
218 To identify mimotopes for FMC63, we employed a yeast surface display library[32]
219 presenting ~$5x10^8$ randomized linear peptides of 10 amino acids (AA, 10mer) for screening
220 against recombinant FMC63 expressed as a full-length IgG (hereafter, $FMC63^{IgG}$, **Fig. 2B**). Initial
221 screening was performed using biotinylated $FMC63^{IgG}$ attached to streptavidin beads for magnetic
222 enrichment of weakly-bound yeast clones. After a single round of screening using this enrichment
223 protocol, flow cytometry analysis identified two yeast populations P1 and P2, which bound with
224 higher or lower relative affinity to $FMC63^{IgG}$, respectively, but not an isotype control antibody (**Fig.**
225 **2C**). The two peptides shared a common enriched sequence motif RXCPWXCXXX. The presence
226 of two cysteines in the mimotope motif suggested the possibility that these mimotopes formed an
227 intramolecular disulfide bond, with the proline between the two cysteines likely promoting a hairpin
228 in the peptide structure[33]. Computational modeling of P1 (RHCPWNCSLL) and P2
229 (RICPWSCRAP) interactions with FMC63 using AlphaFold predicted the mimotopes take on a
230 curved alpha helical structure, suggesting the formation of a cyclic structure with an intra-peptide
231 disulfide bond (**Fig. 2D**).
232 To confirm the presence of a disulfide bond within the mimotope and test whether the
233 disulfide is necessary for peptide binding to $FMC63^{IgG}$, we treated the yeast clone P1 with
234 increasing concentrations of the reducing agent dithiothreitol (DTT, **Fig. 2E**). Treatment with 10
235 mM DTT lowered Aga2p levels on the yeast cells by ~10-fold, likely due to cleavage of the
236 disulfide linkages anchoring the protein to the yeast cell surface. However, mild reductive
237 conditions (i.e., 0.1mM, 1mM DTT) largely preserved Aga2p on yeast surface but eliminated
238 $FMC63^{IgG}$ binding (**Fig. 2E**). To further verify that this loss in antibody binding reflected loss of a
239 disulfide in the mimotope itself, we chemically synthesized a cyclic version of mimotope P1 and
240 monitored its binding to $FMC63^{IgG}$ using ELISA in the presence or absence of pre-treatment of
241 the peptide with DTT, and found that $FMC63^{IgG}$ recognized plate-bound P1 with an estimated K_D
242 of 1.4 μM, but this binding was completely ablated for DTT-treated P1 (**Fig. 2F**).
243 Next, we created amph-mimotope molecules by conjugating P1 functionalized with an N-
244 terminal azide to DSPE-PEG2k-DBCO through click chemistry (**Fig. 2G**). To test whether the
245 amph-mimotope could insert in cell membranes and enable CD19 CAR-T cell recognition, we
246 incubated CD19-negative K562 cells with amph-P1to allow cell association, washed the cells, and
247 then incubated them with human CD19 CAR-T cells *in vitro* (**Fig. 2G**). As shown in **Fig. 2H**, co-
248 culture of CD19 CAR-T with K562 cells decorated by amph-P1 but not a control amph-peptide
249 (pepvIII, a minimal epitope from EGFRvIII) triggered robust IFN-γ secretion from the CAR-T cells.
250 Consistent with the need for the P1 to contain an intramolecular disulfide for CAR recognition,
251 CAR-T stimulation was lost when amph-P1-labeled cells were pre-treated with DTT (**Fig. 2H**). By
252 contrast, control EGFRvIII CAR-T cells had no response to amph-P1 decorated K562 cells

irrespective of the disulfide bond (**Fig. 2I**). These results confirmed that P1 is a functional mimotope with a cyclic conformation required for its specific recognition by FMC63.

To demonstrate that the yeast mimotope library is suitable for identifying mimotopes for any desired antibody, we repeated the library screen using an anti-mouse CD19 antibody (Clone 1D3) (**Extended Data Fig. 4A-D**) and an anti-human Anaplastic Lymphoma Kinase (ALK) antibody of interest for CAR-T cell treatment of lymphoma and some lung cancers (**Extended Data Fig. 4E-F**). These additional library screens successfully identified multiple binders for each antibody, highlighting the potential of yeast surface display to effectively identify antibody-specific mimotope peptides.

Affinity maturation of the CD19 mimotope

The affinity of a typical CAR toward its ligand is often low nanomolar[34], however, mimotope P1 only exhibited a low micromolar apparent affinity toward $FMC63^{IgG}$. We therefore aimed to further evolve the mimotope to obtain variants with enhanced affinity. To this end, we generated a new mimotope library V2 bearing a shared motif derived from the two parental mimotopes, namely RXCPWXCXXX, with a diversity of ~$1.5x10^8$ (**Fig. 3A**). A significant portion of the library V2 could be positively stained with 20 nM biotinylated $FMC63^{IgG}$ while the original P1 yeast clone showed no detectable binding at this concentration (**Fig. 3B**). Flow cytometry sorting of the top 1% of the positive yeast cells followed by Sanger sequencing yielded dozens of mimotope clones. Sequence analysis of these mimotopes revealed a consensus sequence with high-affinity binding potential to $FMC63^{IgG}$ (**Fig. 3C**). Several candidate mimotope clones resembling the consensus sequence were validated experimentally, and all of them exhibited stronger binding than the original clone P1 (**Fig. 3D**). We moved forward with mimotope F12 given its highest resemblance to the consensus sequence and highest binding affinity to $FMC63^{IgG}$ (apparent K_D = 15.6 nM). Alanine scanning across all AA positions in the peptide confirmed the determining role of R at position 1°, C at positions 3° and 7°, P at position 4°, and W at position 5° (**Fig. 3E**). Residues at the remaining AA positions contributed more modestly to the overall affinity. Interestingly, inserting an extra 1-2 alanines between position 6° and 7° completely disrupted F12 binding to FMC63 (**Fig. 3E**), likely through the disruption of the intra-mimotope disulfide bond. Given the labile nature of the disulfide bond in the mimotope, we sought to test if the disulfide bond can be replaced with a structurally similar yet non-reducible thioacetal bond to produce a more stable mimotope (**Extended Data Fig. 5A-B**). Replacing the disulfide bond with a thioacetal bond completely eliminated its binding to $FMC63^{IgG}$, perhaps because the thioacetal bond is 0.9 angstrom (Å) longer than the disulfide bond (**Extended Data Fig. 5C**).

Next, we sought to evaluate the contribution of the flanking sequence to mimotope binding with $FMC63^{IgG}$. A 17 AA linker $(GGGGS)_3AS$ was initially introduced between the 10-mer mimotope and Aga2p during yeast library construction to avoid steric hinderance. We chemically synthesized F12 mimotope variants with increasing length of the upstream linker and performed ELISA to verify $FMC63^{IgG}$ binding. Strikingly, the addition of even a minimal SAS tri-amino acid linker at the N-terminus of the peptide increased binding of F12 to $FMC63^{IgG}$ by ~100-fold (**Fig. 3F**). Given the importance of flanking sequence on mimotope binding to $FMC63^{IgG}$, we created a third yeast library V3 with ~$1x10^8$ diversity with 0-6 and 3-10 flanking residues extended from the N- and C-termini of F12, respectively (**Fig. 3G**), aiming to identify mimotope variants with even higher affinity. We performed kinetic sorting by competing off pre-bound biotinylated monovalent $FMC63^{scFv}$ using non-modified bivalent $FMC63^{IgG}$, and were able to identify yeast populations with prolonged retention of biotinylated $FMC63^{scFv}$, indicative of slower off-rates. Characterization of individual clones identified mimotope variants with further increased affinity compared to the parental F12 clone (**Fig. 3H**). Notably, clone F12-A1 exhibited a further ~10-fold increased affinity toward $FMC63^{scFv}$ compared to F12. In the same competition assay as depicted in **Fig. 3G**, $FMC63^{scFv}$ remained bound on F12-A1 yeast surface over 24 hours in the presence of excess

soluble FMC63^{IgG}, but was competed off the parental F12 clone within half an hour (**Fig. 3I**). Thus, these sequential affinity maturation screens effectively enabled identification of mimotopes with much-improved affinity for the CAR antibody.

Optimized mimotopes bind to FMC63 without compromising its recognition of CD19

To gain a comprehensive view of how the CD19 mimotope interacts with FMC63, we leveraged a recently solved crystal structure of FMC63^{scFv} in complex with CD19 (PDB:7URV)[30] and modeled mimotope binding to FMC63^{scFv}. Both F12 and F12-A1 were modeled using Alphafold[35] and Rosetta[36], and the FMC63^{scFv}-CD19, FMC63^{scFv}-F12, and FMC63^{scFv}-F12A1 binding interfaces were analyzed using PDBePISA[37]. PDBePISA analysis recovered many of the previously defined interactions between FMC63^{scFv} and CD19 through analysis of polarities and bond lengths **(Fig. 4A),** confirming the validity of PDBePISA in performing interaction interface analysis. Structural modeling of F12 (**Fig. 4B**) or F12-A1 (**Fig. 4C**) interactions with FMC63^{scFv} showed that these mimotopes engage FMC63^{scFv} at the same domain. The key residues on FMC63^{scFv} that are essential for CD19 binding were found to be Y260, Y261, Y70, G263, W212, G262, S214, K69, Y265, and G129 [30]. Of these key residues, both F12 and F12-A1 engage Y260 and S214 **(Fig. 4D)**. However, only F12-A1 engages G263 (**Fig. 4D**), which likely explains its stronger binding to FMC63^{scFv} than F12.

To experimentally assess potential overlaps in the binding interface of FMC63 to CD19 vs. our mimotope peptides, we pre-blocked FMC63^{scFv}, FMC63^{IgG} or an alternative control anti-CD19 antibody HIB19^{IgG} with increasing concentrations of mimotopes F12 or F12-A1, and then added the antibody to CD19^{+} NALM6 cells (**Fig. 4E**). When FMC63^{scFv} was pre-blocked with F12 peptide, binding to NALM6 cells was only compromised when the F12 concentration was 100 μM, and NALM6 binding was nearly unaffected for FMC63^{IgG}. By contrast, F12-A1 abolished FMC63^{scFv} or FMC63^{IgG} binding to CD19 when the mimotope concentrations were greater than 1 or 10 μM, respectively, consistent with its higher affinity for FMC63. However, when FMC63 CAR-expressing Jurkat T cells were pre-blocked with increasing concentrations of F12 or F12-A1 and stimulated with NALM6 cells, CD69 induction on Jurkat cells was not affected (**Fig. 4F**). Thus, despite some ability of the mimotopes to interfere with soluble FMC63 binding to CD19^{+} cells at high concentrations, FMC63 CAR-T cells retained their full potential of recognizing CD19^{+} leukemic cells even in the presence of mimotopes.

Amph-mimotope vaccination triggers FMC63-mCAR-T expansion *in vivo*

To test if amph-mimotope vaccines could efficiently stimulate CD19 CAR-T cells in an immunocompetent mouse model *in vivo*, we established a hybrid CAR by fusing the human FMC63 scFv to murine CAR signaling domains, (FMC63-mCAR, **Fig. 5A**). First, we validated the ability of the amph-mimotope variants to stimulate FMC63-mCAR T cells. K562 cells were pre-labeled with amph-mimotope variants and co-cultured with FMC63-mCAR-T cells as in **Fig. 2G.** Amph-mimotope-decorated target cells triggered IFN-γ production from the CAR-T cells, with the stimulation efficiency positively correlating with FMC63-mimotope affinity and amph-F12-A1 providing the strongest CAR-T activation, comparable to stimulation by CD19^{+} NALM6 cells (**Fig. 5B**). To determine if these amph-mimotopes could be effectively presented by DCs *in vivo*, we vaccinated C57BL/6 mice with 10 nmol amph-F12-A1, a dose we previously found to be effective for amph-peptide stimulation of CAR-T cells. We formulated the mimotope with or without cyclic-di-GMP, a STING agonist added as an adjuvant[38]. Following vaccination, we isolated CD11b^{+} myeloid cells and CD11c^{+} DCs from the draining inguinal lymph nodes and analyzed the presence of surface-displayed amph-peptides using flow cytometry by staining the cells with biotinylated FMC63^{IgG} (**Extended Data Fig. 6A**). Interestingly, high levels of amph-mimotope were detected

351 on APCs for at least 24 hr, but only when amph-mimotope was co-administered with adjuvant
352 (**Fig. 5C**).
353 Next, we labeled FMC63-mCAR cells with cell trace violet (CTV) and transferred them into
354 C57BL/6 mice, followed by vaccination with amph-P1, amph-F12, amph-F12-A1 vaccine, or saline
355 as a control, followed by flow cytometry analysis to detect CAR-T cell proliferation (CTV dilution)
356 2 days later. This functional test of amph-mimoptope stimulation revealed a clear hierarchy of
357 mimotope activity *in vivo*, with amph-P1 eliciting no CAR-T cell division, amph-F12 eliciting limited
358 proliferation, and only amph-F12-A1 triggering proliferation of the entire CAR-T population (**Fig.**
359 **5D**). These data suggest there is an affinity threshold for mimotope vaccines to effectively
360 stimulate CAR-T cells *in vivo*.
361 Clinical evidence indicates that lack of antigen exposure soon after adoptive transfer may
362 compromise CAR-T engraftment[39]. To test if amph-mimotope vaccine boosting post adoptive cell
363 transfer could promote FMC63-mCAR-T cell expansion and engraftment in the absence of
364 leukemia, naïve CD45.2$^+$ C57BL/6 mice received sublethal lymphodepletion followed by
365 intravenous infusion of either CD45.1$^+$ FMC63-mCAR-T or control untransduced T cells (**Fig. 5E**).
366 Without additional treatment, peripheral CD45.1$^+$ CAR-T cells only occupied <5% of total CD8$^+$ T
367 cells by day 4 and decreased to <3% by day 14 (**Fig. 5E**). By contrast, amph-F12-A1 vaccine
368 boosting rapidly amplified CD45.1 CAR-T cells, reaching ~40% of total peripheral CD8$^+$ T cells
369 (~500 CAR-T cells per microliter of blood, **Fig. 5E, Extended Data Fig. 6B**) by day 14 after two
370 doses of vaccination, and then slowly contracting over the next few weeks.
371
372 **Amph-mimotope-labeled DCs enhance human CD19 CAR-T expansion and leukemia**
373 **clearance in a humanized mouse model**

374 Human CAR-T cells are routinely evaluated in immunodeficient NSG mice, but this animal model
375 is problematic for testing lymphatic-mediated amph-vaccine boosting, as these mice have
376 generally defective lymph node and lymphatic development due to their lack of native
377 lymphocytes[40]. To overcome this technical hurdle, we devised an alternate strategy to test amph-
378 vaccine boosting of human CAR-T cells: We previously showed that amph-ligand vaccine
379 molecules label lymph node-resident DCs, which are the key APC population mediating the amph-
380 vaccine stimulation[14]. To mimic this process in NSG mice in a human-relevant setting, we
381 differentiated human peripheral blood monocytes into DCs *in vitro* and matured them with
382 lipopolysaccharide (LPS) and IFN-γ (**Fig. 6A**). These matured human monocyte-derived DCs
383 (MoDCs) exhibited significantly increased expression of multiple co-stimulatory molecules,
384 including CD80/86, 41BBL, Ox40L, and ICOSL (**Fig. 6A**). Incubation of activated MoDCs with
385 amph-F12-A1 led to robust cell surface labeling with the mimotope (DC-mVax, **Fig. 6B**) and
386 efficiently stimulated human CD19 CAR-T cell activation *in vitro* (**Fig. 6C**). To determine if DC-
387 mVax could activate and expand human CD19 CAR-T cells *in vivo* in the absence of additional
388 antigen, we intravenously (i.v.) infused human CD19 CAR-T cells into non-leukemic NSG mice
389 with or without subsequent i.v. infusion of DC-mVax (**Fig. 6D-E**). Mice receiving a single dose of
390 DC-mVax 24 hours post CAR-T infusion exhibited significant expansion of CAR-T cells in the
391 peripheral blood compared to those receiving unmodified DCs, and circulating human CD19 CAR-
392 T cells remained detectable at day 30 (**Fig. 6E**). Notably, the extent of CAR-T cell expansion
393 markedly decreased when DC-mVax was infused 7 days post CAR-T cell transfer, indicating that
394 early antigen exposure plays an important role in promoting CAR-T expansion and engraftment
395 (**Fig. 6E**). Repeated dosing of DC-mVax on day 1 and day 7 days led to a further increase in CAR-
396 T cell expansion (**Fig. 6E**).
397 To determine if DC-mVax boosting could augment the anti-tumor activity of human CD19
398 CAR-T cells, we established leukemia in NSG mice by infusion of luciferase-expressing NALM6
399 tumor cells as previously described[41]. Suboptimal doses of CD19 CAR-T cells were administered
400 on day 4 followed 24 hours later by repeated i.v. infusion of either unmodified DCs or DC-mVax

401 (**Fig. 6F**). Despite the presence of high levels of target cells, CAR-T cells alone showed poor
402 persistence/expansion compared to CAR-T cells boosted with DC-mVax (**Fig. 6G**). While CAR-T
403 cells alone only slightly delayed tumor expansion and moderately prolonged survival, addition of
404 the DC-mVax boosting enabled this dose of CAR-T cells to substantially slow tumor growth and
405 30% of the animals completed rejected their tumors (**Fig 6H-J**). Collectively, these results
406 demonstrated that a suitably affinity-matured amph-mimotope could act as an effective vaccine
407 to promote engraftment, expansion and reinvigoration of human T cells expressing the CAR
408 currently used in all approved CD19-targeting CAR-T products, and enhance their anti-leukemic
409 activity.
410

411 **Discussion**

412 Successful engraftment and persistence is critical for ensuring robust and long-term anti-leukemic
413 activity by CAR-T cells[1,42]. Analysis of data from recent CAR-T cell clinical trials suggested that
414 CD19-directed CAR-T cells initially expand more strongly if there is a high tumor burden,
415 consistent with the idea of CAR-T expansion that is commensurate with the dose of antigen
416 encountered. However, long-term persistence of CAR-T cells does not correlate with initial tumor
417 burden, suggesting that this initial stimulus vanishes over time as leukemic cells are cleared from
418 the body and/or that stimulation received from tumor cells or naïve B cells lacking appropriate
419 costimulatory signals is insufficient to maintain the CAR-T cell population. We and others have
420 recently demonstrated the ability of using a synthetic vaccine to boost CAR-T cells *in vivo* and
421 achieved enhanced therapeutic outcomes[14,15,43]. Our strategy of linking a ligand for the CAR to a
422 lymph node-targeting PEG-lipid amphiphile is simple, but requires a suitable peptide or protein
423 ligand. The poor expression and folding of recombinant human CD19 ectodomain[29] makes use
424 of the native target antigen impractical for this approach. Here we demonstrate that surrogate
425 CAR ligands based on short peptides can be readily identified and affinity matured using directed
426 evolution, enabling the generation of mimotope vaccines that efficiently boost CD19 CAR-T cells
427 analogous to natural CD19 antigen exposure. Vaccine boosting significantly impacted the
428 outcome of CD19 CAR-T cell therapy by increasing CAR-T cell expansion and engraftment, and
429 we have shown previously, also augments CAR-T cell functionality. Importantly, the mimotope
430 vaccine discovered here is applicable to all four FDA-approved FMC63-based CD19 CAR-T cell
431 therapies.
432 In addition to the human CD19 CAR mimotope, mimotopes for anti-mouse CD19 and anti-
433 human ALK CARs were also successfully identified using the same yeast mimotope library,
434 indicating the broad applicability of this library for identifying mimotopes for any desired antibody.
435 Experimental verification and structural modeling demonstrated that the CD19 mimotope
436 discovered through the yeast library forms a cyclic conformation that is essential for its recognition
437 by FMC63. Given that FMC63 recognizes a conformational epitope, it is possible that a mimotope
438 also needs to form a desired secondary structure to achieve strong binding. Notably, the CD19
439 mimotope only partially occupies the natural epitope binding domain on FMC63. This partial
440 occupancy appears to enable FMC63-based CD19 CAR-T cells to maintain their capacity to
441 recognize $CD19^+$ leukemia cells even in the presence of the mimotope, which could be important
442 for allowing the CAR-T cells to continue to sense tumor cells in lymph nodes during vaccine
443 boosting. The transient surface presentation of amph-ligands also prevents CAR-T cells from
444 receiving excessive and prolonged antigen exposure, thus reducing the likelihood of CAR-T cell
445 exhaustion and severe cytokine release syndrome[14].
446 Despite expansion and efficacy of CD19 CAR-T cells following the first infusion, reinfusion
447 of CAR-T cells into patients experiencing $CD19^+$ tumor relapse is often ineffective, with
448 significantly lower CAR-T expansion compared to the first infusion[39,44–46]. While B cells retain the
449 antigen for CAR-T, evidence suggests that B cells themselves may not be as effective as
450 conventional DCs for restimulating CAR-T cells at least partially due to greater expression of co-

stimulatory molecules in DCs[26]. Our previous findings showed that costimulatory molecules expressed by activated DCs are crucial for optimally expanding CAR-T cells with amph-ligands[14]. Therefore, one potential use of the mimotope vaccine is to support CAR-T cells during reinfusion. Notably, even during the first infusion, CD19 CAR-T cells rapidly decline after a transient expansion[9,47]. Despite the general correlation of initial CAR-T expansion with baseline tumor burden, a long-term follow-up study in B-ALL found that a higher ratio of peak CAR-T-cell expansion to tumor burden significantly correlated with event-free survival and overall survival[23]. Although this effective ratio more likely occurs in patients with lower tumor burden, administering the mimotope vaccine upon CAR-T contraction during the first infusion could potentially reinvigorate CAR-T cells and sustain CAR-T expansion to elevate this effective ratio in patients with both low and high tumor burden to improve event-free survival.

One shortcoming of characterizing vaccines for human T cells is the lack of proper humanized mouse models. The defective lymphatics, absent or disorganized lymph nodes, and poor crosstalk of mouse APCs with human T cells is a barrier to evaluating vaccine boosting of human CAR-T cells in NSG mice[40]. As an alternative, we evaluated vaccine boosting of mouse T cells bearing a hybrid FMC63-mCAR in immunocompetent C57BL/6 mice via standard vaccine administration routes, and boosting of human CD19 CAR-T cells using mimotope-decorated human MoDCs in NSG mice via i.v. delivery. These two complementary approaches demonstrated the feasibility of the mimotope vaccine in both the setting of natural trafficking and distribution from lymphatics to lymph nodes as well as its capacity in stimulating human CAR-T cells upon insertion into the surface of human DCs.

mRNA vaccines encoding the target tumor antigen can also be employed to stimulate CAR-T cells[43]. Recently, an CLDN6-expressing mRNA vaccine was tested in a phase 1 clinical trial in combination with CLDN6-directed CAR-T cells and showed promise in improving CAR-T cell expansion in patients with solid tumors[48]. Importantly, CAR-T plus mRNA vaccination was well tolerated, suggesting the overall safety profile associated with this combination therapy. However, mRNA-LNPs differ from our amphiphile vaccines in their *in vivo* trafficking, biodistribution, and the duration of antigen presentation on cell surface, therefore their differential effects on boosting human CD19 CAR-T cells remain to be determined and is beyond the scope of this work.

In summary, we have designed and validated a general strategy to generate mimotope ligands for any CAR T cell. Using this methodology, we demonstrate an amph-mimotope vaccine that could be used clinically in tandem with all four FDA-approved CD19 CAR-T cell products. The ability of amph-mimotope vaccines to efficiently stimulate human CD19 CAR-T cells *in vivo* support its potential use as a robust and clinically-translatable approach for enhancing the engraftment, long-term persistence, and anti-leukemic activity of current CD19 CAR-T cell therapies.

ACKNOWLEDGMENTS

We thank the Koch Institute Swanson Biotechnology Center for technical support, specifically the flow cytometry core facility. **Funding:** This work was supported by the NIH (award EB022433 to DJI), the Marble Center for Nanomedicine (to DJI), and the Mark Foundation for Cancer Research (to DJI). L.M was supported by an American Cancer Society postdoctoral fellowship, the Cell and Gene Therapy Collaborative and the Junior faculty pilot program at CHOP, NIH New Innovators Award (DP2 AI164319-03), ITMAT at UPenn and NCATS (UL1TR001878). This work is also partially supported by Cancer Center Support (core) Grant P30-CA14051 from the NCI to the Barbara K. Ostrom (1978) Bioinformatics and Computing Core Facility of the Swanson Biotechnology Center. D.J.I. is an investigator of the Howard Hughes Medical Institute. R.R. is supported by a National Science Foundation Graduate Research Fellowship Program award. Parisa Yousefpour is supported by an NRSA F32 fellowship (award AI164829) from the NIH. M.R. is supported by the NIH NCI P01 PCA214278C, the R01/37-CA262362-01A1, the Laffey McHugh Foundation, and the Berman and

Maguire Funds for Lymphoma Research at Penn. G.G is supported by the SITC-Mallinckrodt Pharmaceuticals Adverse Events in Cancer Immunotherapy Clinical Fellowship, and the Mario Luvini fellowship grant—Fondazione Ticinese per la Ricerca sul Cancro.

Data and materials availability: All data are available on request.

AUTHOR CONTRIBUTIONS

L.M., D.J.I. and K.D.W designed the studies. L.M. R.R. D.J.I. analyzed and interpreted the data and wrote the manuscript. L.M and N.M generated yeast mimotope libraries. L.M. performed the experiments. B.C and I.S assisted with mimotope identification. D.M.M. mined single cell RNA-sequencing data. L.M. and L.Z. carried out amphiphile-mimotope synthesis. R.R performed structural modeling. I.S. P.Y. and H.S. assisted with sample preparation. W.A. T.M.M. and A.C. assisted with animal experiments. S.K, R.M.M, S.A.G, L.P, G.G., S.J.S, N.F and M.R processed and provided the clinical data.

DECLARATION OF INTERESTS

L.M and D.J.I are inventors on patents filed related to the amphiphile-mimotope vaccine technology. G.G. served as a scientific consultant for viTToria Biotherapeutics. M.R. holds patents related to CD19 CAR-T cells, served as a consultant for NanoString, Bristol Myers Squibb,GlaxoSmithKline, Scaylite, Bayer, and AbClon, receives research funding from AbClon,NanoString, Oxford NanoImaging, viTToria biotherapeutics, CURIOX, and Beckman Coulter. M.R. is the scientific founder of viTToria Biotherapeutics

552 **FIGURE LEGENDS**
553
554 **Figure 1: CD19 CAR-T cell expansion and B cell aplasia in patients with initial high (≥40%)**
555 **or low tumor burden (<40%), and rationale for a DC-targeting CD19-CAR stimulating**
556 **vaccine**. (**A**) Scatterplot of peripherally circulating CAR-T cells measured by quantitative
557 polymerase chain reaction (qPCR) over time during the first month after infusion. Solid lines show
558 trends generated by locally estimated scatterplot smoothing (loess). The median time to peak
559 CAR-T expansion was 10 days after infusion in both cohorts. (**B**) Maximum concentration and (**C**)
560 Area under the curve (AUC) of CAR-Transgene levels measured by qPCR, broken down by tumor
561 burden. ***, p<0.001, by Wilcoxon rank-sum tests. (**D**) Kaplan-Meier analysis of B cell aplasia for
562 all patients (black) or high (orange) or low (blue) tumor burden patients. B cell aplasia is defined
563 as the time to the emergence of ≥1% CD19-positive B cell in bone marrow aspirate or ≥3% B cell
564 by peripheral blood flow cytometry or CD19-positive relapse. Data were censored for patients
565 who had CD19-negative relapse, reinfusion for hematogones in the marrow, alternative therapy
566 including other CAR-T therapy or hematopoietic stem cell transplant, or non-relapse mortality. The
567 probability of continued B-cell aplasia at two years was similar in both cohorts (p = 0.76). At 6
568 months, it was 72% (95% CI 55-95) in high and 67% (95% CI 57-78) in low tumor burden patients.
569 (**E**) Box plot of costimulatory molecule module scores expressed by B cells (likely-healthy and
570 likely-malignant) and DC. Each point represents the average of all cells of that phenotype within
571 a patient. ****, p<0.0001, by a two-sided Wilcoxon rank-sum test.
572
573 **Figure 2: Yeast surface display identifies CD19-CAR binding mimotopes.** (**A**) Illustration of
574 CD19-CAR stimulation by natural CD19 or amph-mimotope. (B) Yeast surface display workflow
575 for identifying antibody-specific mimotopes. (**C**) Flow cytometry plots showing the successful
576 identification of yeast cell populations (P1 and P2) binding to 1 μM $FMC63^{IgG}$ after a single round
577 of magnetic enrichment. (**D**) Structural modeling of mimotopes P1 and P2 binding to FMC63. (**E**)
578 Yeast cells bearing mimotope P1 was treated with increasing concentrations of DTT, and then
579 stained with 500 nM biotin-$FMC63^{IgG}$ and an anti-HA tag antibody for analysis of binding by flow
580 cytometry. (**F**) ELISA analysis showing the impact of the disulfide bond on $FMC63^{IgG}$ binding to
581 plate-bound P1 mimotope. (**G**) Scheme for amph-mimotope generation by click chemistry linkage
582 of azide-modified P1 to DBCO-PEG-DSPE, and schematic illustration of amph-P1 coating of
583 target cells. (**H-I**) $CD19^-$ K562 cells were labeled with control amph-pepvIII or amph-P1 molecules
584 *in vitro* followed with or without 1μM DTT treatment and subsequent co-culture with human CD19
585 CAR-T cells (**H**) or EGFRvIII CAR-T cells (**I**). IFN-γ ELISA was performed to monitor activation of
586 CAR-T cells. Error bars show mean ± s.d. with triplicate samples. **, p<0.01 by one-way ANOVA
587 with Turkey's post-test. A, B and G are created with BioRender.com.
588
589 **Figure 3: Affinity maturation of CD19 mimotopes.** (**A**) Schematic workflow for identifying
590 affinity-enhanced mimotope variants of P1 from a motif-fixed mimotope library V2. Created with
591 BioRender.com. (**B**) Flow cytometry plots of 20 nM FMC63IgG binding to yeast cells expressing
592 the V2 mimotope library. Yeast cells bearing mimotope P1 was included as a control. (**C**) Weblogo
593 showing the consensus mimotope sequence with high-affinity binding to $FMC63^{IgG}$. (**D**) Binding
594 of $FMC63^{IgG}$ to select yeast clones assessed by flow cytometry. Amino acid sequences and
595 apparent binding affinity are shown for each yeast clone. (**E**) Yeast clones bearing F12 variants
596 with 1-2 alanine (Red) insertions or individual AA mutated to alanine (Red) were assessed for
597 $FMC63^{IgG}$ binding by flow cytometry. (**F**) ELISA showing the impact of flanking residues on
598 $mimotope^{F12}$ binding to $FMC63^{IgG}$. The apparent binding affinity was determined as in D. (**G**)
599 Schematic workflow for identifying affinity-enhanced mimotopes from mimotope library V3 using
600 kinetic sorting. Yeast library V3 were first stained with monovalent biotin-$FMC63^{scFv}$ followed by
601 competition with non-biotinylated bivalent $FMC63^{IgG}$. Created with BioRender.com. (**H**) Binding of

602 FMC63^{scFv} to select yeast clones bearing various flanking sequences. The parental mimotope^{F12}
603 sequence was underlined. Apparent binding affinity was determined as in D. (**I**) Representative
604 histograms showing retention of prebound FMC63^{scFv} on yeast clone F12-A1 in the presence of
605 FMC63^{IgG}. Yeast cells were pre-stained with 50nM Biotin-FMC63^{scFv} followed by incubation with
606 1μM FMC63^{IgG}. Yeast cells were sampled at indicated times for PE-streptavidin staining as an
607 indicator for the retention of Biotin-FMC63^{scFv}.
608
609 **Figure 4: Structural modeling of mimotopes complexed with FMC63. (A)** Ribbon diagram of
610 FMC63^{scFv} (purple) in complex with human CD19 (green, PDB 7URV). Interactions involving key
611 residues of FMC63 are shown. Interacting sidechain atoms are shown and boxed. Interactions
612 involving backbone atoms are labeled without box. **(B-C)** Computational models generated using
613 Alphafold and Rosetta for FMC63^{scFv} bound to F12 (**B**) or F12-A1 (**C**), respectively. Interactions
614 involving previously mentioned key residues of FMC63 are labeled using same scheme as in A.
615 For F12-A1, the orientation of mimotope is shown to best exhibit how it engages FMC63. The
616 panel in the bottom left depicts the complex in the same orientation as F12-FMC63. **(D)** Interface
617 footprint of mimotopes on FMC63. On the left side, the CD19 interface is shown in green, the F12
618 interface shown in orange, and overlapping residues are shown in red. On the right side, the CD19
619 interface is shown in green, the F12A1 interface shown in blue, and overlapping are residues
620 shown in red. **(E)** Biotinylated FMC63^{scFv} was pre-incubated with various concentrations of F12
621 or F12-A1 prior to staining NALM6 cells and detection via PE-conjugated streptavidin. For
622 FMC63^{IgG} binding, NALM6 cells were stained with the same concentrations of mimotope and
623 FMC63^{IgG} with no prior incubation, and binding was detected using PE-conjugated anti-mouse-
624 IgG. A non-competing IgG clone HIB19 is shown as control. **(F)** FMC63 CAR^{+} Jurkat T cells were
625 pre-incubated with F12 or F12-A1 at indicated concentrations, then co-cultured with NALM6 cells
626 at a 1:1 ratio for 16 hours followed by flow cytometry analysis of CD69 expression. Shown in E-F
627 are one representative results of three independent experiments.
628
629 **Figure 5: Amph-mimotopes require a threshold affinity to stimulate CAR-T proliferation in**
630 **vivo**. (**A**) Schematic of hybrid FMC63-mCAR design. (**B**) K562 cells were labeled with 100 nM of
631 amph-mimotope variants for 30 min, washed, and co-cultured with FMC63-mCAR-T cells at a 1:1
632 E:T ratio for 6 hours followed by ELISA measurement of IFN-γ secretion. Error bars show mean
633 ± s.d. with triplicate samples. (**C**) C57BL/6 mice (*n*=3 animals/group) were vaccinated with 10
634 nmol amph-mimotope ± CDN adjuvant, and 24 or 48 hr later, mimotope uptake by macrophages
635 and cDCs was detected by staining with FMC63 followed by flow cytometry analysis. Shown are
636 representative histograms of FMC63 staining. (**D**) C57BL/6 mice (*n*=3 animals/group) were
637 lymphodepleted, adoptively transferred with $2x10^6$ CTV-labeled CAR-T cells, then vaccinated 1
638 day later with 10 nmol amph-peptides + CDN adjuvant. Shown are representative histograms of
639 FMC63-mCAR-T cell proliferation in LNs 48 hours after vaccination. (**E**) C57BL/6 mice (*n*=5
640 animals/group) were lymphodepleted (L.D.), adoptively transferred with 10^6 FMC63 CAR-T cells,
641 and then vaccinated at indicated time points, and circulating FMC63-mCAR-T cells were
642 quantified in the blood by flow cytometry over time. Error bars show mean ± 95% CI. ***,
643 p<0.0001;**, p<0.01; n.s., not significant by one-way ANOVA with Turkey's post- test for B-D, two-way
644 ANOVA with Tukey's post-test for E.
645
646 **Figure 6: Amph-mimotope vaccine-labeled DCs augment human CD19 CAR-T therapy**
647 **against leukemia.** (**A**) Schematic of approach to generate "DC-mVax" and representative
648 histograms depicting LPS/IFNγ-induced upregulation of co-stimulatory markers on mature DCs.
649 (**B**) Activated MoDCs were incubated with 500 nM amph-F12-A1 or control amph-pepvIII for
650 30min, washed, and then stained with FMC63^{IgG}. Shown are representative histogram of

651 FMC63^{IgG} labeling. (**C**) Activated MoDCs were labeled with amph-F12-A1 or amph-pepvIII as in
652 (B) and then co-cultured human CD19 CAR-T cells at a 1:1 E:T ratio. Shown is IFN-γ measured
653 in the supernatant after 6 hr by ELISA. Error bars show mean ± s.d. with triplicate samples. (**D**)
654 Experimental setup and timeline for E. (**E**) Quantification of circulating human CD19 CAR-T cells
655 in the absence or presence of a single dose of DC-mVax at day 1 or day 7 or two weekly doses
656 of DC-mVax administered following timeline in D (n=5 animals/group). (**F**) Experimental setup and
657 timeline for G-J. (**G-J**) CAR-T cells were administered with or without DC-mVax as shown in
658 timeline (F) and tumor progression (H) was monitored using *in vivo* bioluminescent imaging (*n*=5
659 animals/group. Shown are enumeration of circulating human CD19 CAR-T cells on day 21 (**G**),
660 whole animal imaging at indicated times (**H**) and quantification of total photon counts over time
661 (**I**). Shown is one of two independent experiments. (**J**) NSG mice (*n*=10 animals/group) inoculated
662 with NALM6 tumor cells and treated with CAR-T cells ± DC-mVax as in F were followed for overall
663 survival. Shown are combined data from two independent experiments. Error bars show mean ±
664 95% CI. ***, $p<0.0001$; **, $p<0.01$ by Student's t-test for C and G, by two-way ANOVA with Tukey's
665 post-test for E and I, and by Log-rank (Mantel-Cox) test for J.
666
667
668
669
670

671 **References**
672

673 1. Cappell, K. M. & Kochenderfer, J. N. Long-term outcomes following CAR T cell therapy: what
674 we know so far. *Nat. Rev. Clin. Oncol.* **20**, 359–371 (2023).

675 2. Irvine, D. J., Maus, M. V., Mooney, D. J. & Wong, W. W. The future of engineered immune cell
676 therapies. *Science* **378**, 853–858 (2022).

677 3. Labanieh, L. & Mackall, C. L. CAR immune cells: design principles, resistance and the next
678 generation. *Nature* **614**, 635–648 (2022).

679 4. Bai, Z. *et al.* Single-cell antigen-specific landscape of CAR T infusion product identifies
680 determinants of CD19-positive relapse in patients with ALL. *Sci. Adv.* **8**, eabj2820 (2022).

681 5. Wang, X. & Rivière, I. Clinical manufacturing of CAR T cells: foundation of a promising therapy.
682 *Mol. Ther. - Oncolytics* **3**, 16015 (2016).

683 6. Neeser, A., Ramasubramanian, R., Wang, C. & Ma, L. Engineering enhanced chimeric antigen
684 receptor-T cell therapy for solid tumors. *Immuno-Oncol. Technol.* **19**, 100385 (2023).

685 7. Garfall, A. L. *et al.* T-cell phenotypes associated with effective CAR T-cell therapy in
686 postinduction vs relapsed multiple myeloma. *Blood Adv.* **3**, 2812–2815 (2019).

687 8. Turtle, C. J. *et al.* CD19 CAR–T cells of defined CD4+:CD8+ composition in adult B cell ALL
688 patients. *Journal of Clinical Investigation* **126**, 2123–2138 (2016).

689 9. Kadauke, S. *et al.* Risk-Adapted Preemptive Tocilizumab to Prevent Severe Cytokine Release
690 Syndrome After CTL019 for Pediatric B-Cell Acute Lymphoblastic Leukemia: A Prospective
691 Clinical Trial. *J. Clin. Oncol.* **39**, 920–930 (2021).

692 10. Seder, R. A., Darrah, P. A. & Roederer, M. T-cell quality in memory and protection:
693 implications for vaccine design. *Nat. Rev. Immunol.* **8**, 247–258 (2008).

694 11. Eyquem, J. *et al.* Targeting a CAR to the TRAC locus with CRISPR/Cas9 enhances tumour
695 rejection. *Nature* **543**, 113–117 (2017).

696 12. Rossig, C. *et al.* Vaccination to improve the persistence of CD19CAR gene-modified T cells
697 in relapsed pediatric acute lymphoblastic leukemia. **31**, 1087–1095 (2017).

698 13. Akahori, Y. *et al.* Antitumor activity of CAR-T cells targeting the intracellular oncoprotein WT1
699 can be enhanced by vaccination. *Blood* **132**, 1134–1145 (2018).

700 14. Ma, L. *et al.* Enhanced CAR–T cell activity against solid tumors by vaccine boosting through
701 the chimeric receptor. *Science* **365**, 162–168 (2019).

702 15. Ma, L. *et al.* Vaccine-boosted CAR T crosstalk with host immunity to reject tumors with antigen
703 heterogeneity. *Cell* **186**, 3148-3165.e20 (2023).

704 16. Boder, E. T. & Wittrup, K. D. Yeast surface display for screening combinatorial polypeptide
705 libraries. *Nat. Biotechnol.* **15**, 553–557 (1997).

706 17. Rafiq, S., Hackett, C. S. & Brentjens, R. J. Engineering strategies to overcome the current
707 roadblocks in CAR T cell therapy. *Nat Rev Clin Oncol* **17**, 147–167 (2020).

708 18. Maude, S. L. *et al.* Chimeric antigen receptor T cells for sustained remissions in leukemia.
709 *New Engl J Medicine* **371**, 1507–17 (2014).

710 19. Kadauke, S. *et al.* Risk-Adapted Preemptive Tocilizumab to Prevent Severe Cytokine Release
711 Syndrome After CTL019 for Pediatric B-Cell Acute Lymphoblastic Leukemia: A Prospective
712 Clinical Trial. *J Clin Oncol* JCO.20.02477 (2021) doi:10.1200/jco.20.02477.

713 20. Frey, N. V. *et al.* Optimizing Chimeric Antigen Receptor T-Cell Therapy for Adults With Acute
714 Lymphoblastic Leukemia. *J. Clin. Oncol. : Off. J. Am. Soc. Clin. Oncol.* **38**, 415–422 (2019).

715 21. J., S. S. *et al.* Chimeric Antigen Receptor T Cells in Refractory B-Cell Lymphomas. *N. Engl.*
716 *J. Med.* **377**, 2545–2554 (2017).

717 22. Maude, S. L. *et al.* Chimeric Antigen Receptor T Cells for Sustained Remissions in Leukemia.
718 *New England Journal of Medicine* **371**, 1507–1517 (2014).

719 23. Park, J. H. *et al.* Long-Term Follow-up of CD19 CAR Therapy in Acute Lymphoblastic
720 Leukemia. *N. Engl. J. Med.* **378**, 449–459 (2018).

721 24. Fischer, L. *et al.* Cellular dynamics following CAR T cell therapy are associated with response
722 and toxicity in relapsed/refractory myeloma. *Leukemia* 1–11 (2024) doi:10.1038/s41375-023-
723 02129-y.

724 25. Ho, W. Y., Cooke, M. P., Goodnow, C. C. & Davis, M. M. Resting and anergic B cells are
725 defective in CD28-dependent costimulation of naive CD4+ T cells. *J. Exp. Med.* **179**, 1539–1549
726 (1994).

727 26. Lim, T. S. *et al.* CD80 and CD86 Differentially Regulate Mechanical Interactions of T-Cells
728 with Antigen-Presenting Dendritic Cells and B-Cells. *PLoS ONE* **7**, e45185 (2012).

729 27. Witkowski, M. T. *et al.* Extensive Remodeling of the Immune Microenvironment in B Cell Acute
730 Lymphoblastic Leukemia. *Cancer Cell* **37**, 867-882.e12 (2020).

731 28. Klesmith, J. R., Wu, L., Lobb, R. R., Rennert, P. D. & Hackel, B. J. Fine Epitope Mapping of
732 the CD19 Extracellular Domain Promotes Design. *Biochemistry* **58**, 4869–4881 (2019).

733 29. Laurent, E. *et al.* Directed Evolution of Stabilized Monomeric CD19 for Monovalent CAR
734 Interaction Studies and Monitoring of CAR-T Cell Patients. *ACS Synth. Biol.* **10**, 1184–1198
735 (2021).

736 30. He, C. *et al.* CD19 CAR antigen engagement mechanisms and affinity tuning. *Sci. Immunol.*
737 **8**, eadf1426 (2023).

738 31. Li, N. *et al.* CAR T cells targeting tumor-associated exons of glypican 2 regress neuroblastoma
739 in mice. *Cell Rep. Med.* **2**, 100297 (2021).

740 32. Wellhausen, N. *et al.* Epitope base editing CD45 in hematopoietic cells enables universal
741 blood cancer immune therapy. *Sci. Transl. Med.* **15**, eadi1145 (2023).

742 33. Melnikov, S. *et al.* Molecular insights into protein synthesis with proline residues. *EMBO Rep.*
743 **17**, 1776–1784 (2016).

744 34. Foote, J. & Eisen, H. N. Breaking the affinity ceiling for antibodies and T cell receptors. *Proc.*
745 *Natl. Acad. Sci.* **97**, 10679–10681 (2000).

746 35. Jumper, J. *et al.* Highly accurate protein structure prediction with AlphaFold. *Nature* **596**, 583–
747 589 (2021).

748 36. Rohl, C. A., Strauss, C. E. M., Misura, K. M. S. & Baker, D. Protein Structure Prediction Using
749 Rosetta. *Methods Enzym.* **383**, 66–93 (2004).

750 37. Krissinel, E. & Henrick, K. Inference of Macromolecular Assemblies from Crystalline State. *J.*
751 *Mol. Biol.* **372**, 774–797 (2007).

752 38. Burdette, D. L. *et al.* STING is a direct innate immune sensor of cyclic-di-GMP. *Nature* **478**,
753 515–518 (2011).

754 39. Holland, E. M. *et al.* Efficacy of second CAR-T (CART2) infusion limited by poor CART
755 expansion and antigen modulation. *J. Immunother. Cancer* **10**, e004483 (2022).

756 40. Shultz, L. D., Brehm, M. A., Garcia-Martinez, J. V. & Greiner, D. L. Humanized mice for
757 immune system investigation: progress, promise and challenges. *Nat. Rev. Immunol.* **12**, 786–
758 798 (2012).

759 41. Gordon, K. S. *et al.* Screening for CD19-specific chimaeric antigen receptors with enhanced
760 signalling via a barcoded library of intracellular domains. *Nat Biomed Eng* **6**, 855–866 (2022).

761 42. Melenhorst, J. J. *et al.* Decade-long leukaemia remissions with persistence of CD4+ CAR T
762 cells. *Nature* **602**, 503–509 (2022).

763 43. Reinhard, K. *et al.* An RNA vaccine drives expansion and efficacy of claudin-CAR-T cells
764 against solid tumors. *Science* **367**, 446–453 (2020).

765 44. Gauthier, J. *et al.* Factors associated with outcomes after a second CD19-targeted CAR T-
766 cell infusion for refractory B-cell malignancies. *Blood* **137**, 323–335 (2021).

767 45. Myers, R. M. *et al.* Outcomes after Reinfusion of CD19-Specific Chimeric Antigen Receptor
768 (CAR)-Modified T Cells in Children and Young Adults with Relapsed/Refractory B-Cell Acute
769 Lymphoblastic Leukemia. *Blood* **138**, 474 (2021).

770 46. Wagner, D. L. *et al.* Immunogenicity of CAR T cells in cancer therapy. *Nat. Rev. Clin. Oncol.*
771 **18**, 379–393 (2021).

772 47. Faude, S. *et al.* Absolute lymphocyte count proliferation kinetics after CAR T-cell infusion
773 impact response and relapse. *Blood Adv.* **5**, 2128–2136 (2021).

774 48. Mackensen, A. *et al.* CLDN6-specific CAR-T cells plus amplifying RNA vaccine in relapsed or
775 refractory solid tumors: the phase 1 BNT211-01 trial. *Nat. Med.* **29**, 2844–2853 (2023).

776

Fig 1

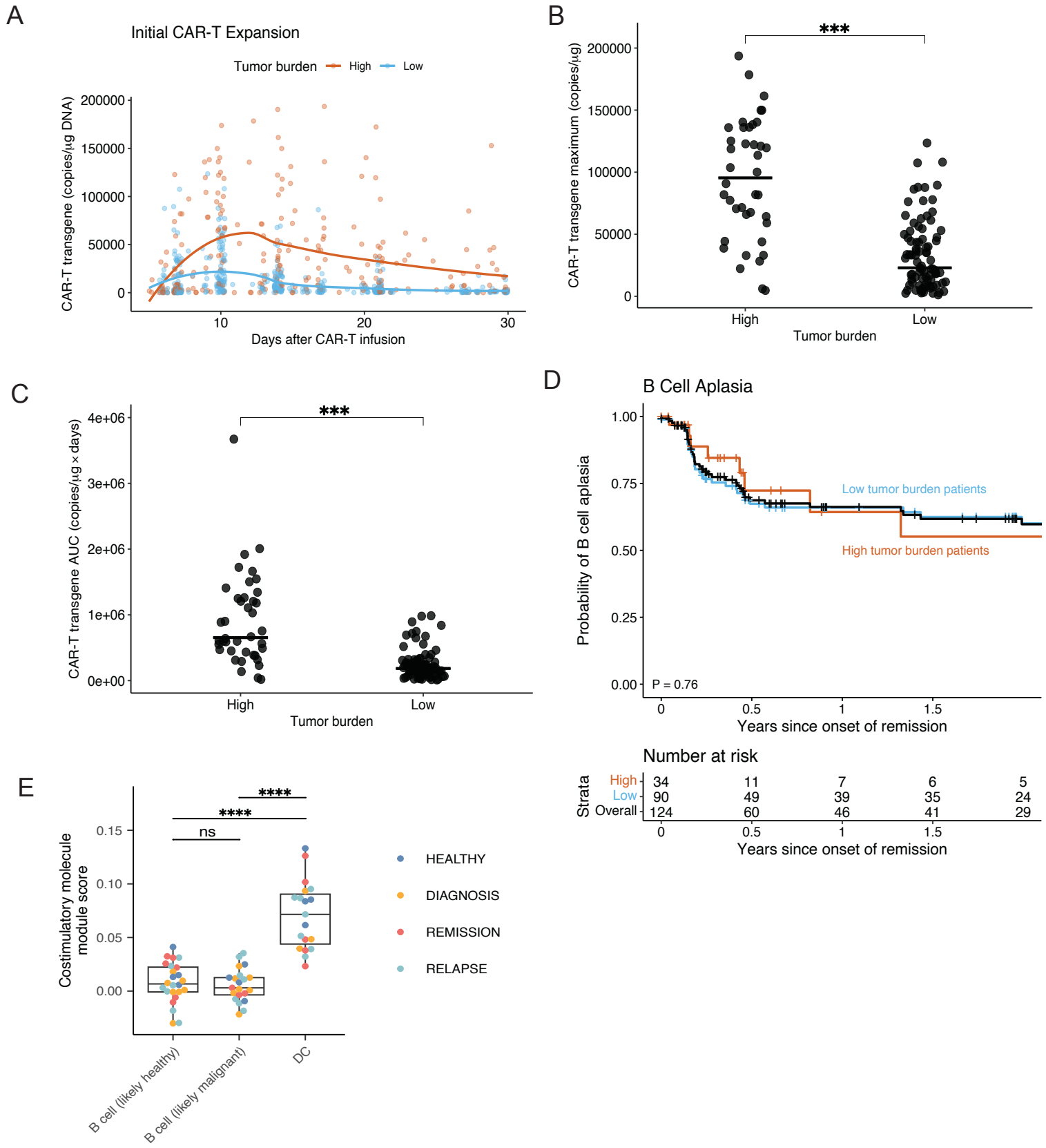
A
Initial CAR-T Expansion
Tumor burden
High
Low
CAR-T transgene (copies/μg DNA)
200000
150000
100000
50000
0
10
20
30
Days after CAR-T infusion
B
***
CAR-T transgene maximum (copies/μg)
200000
150000
100000
50000
0
High
Low
Tumor burden
C
***
CAR-T transgene AUC (copies/μg × days)
4e+06
3e+06
2e+06
1e+06
0e+00
High
Low
Tumor burden
D
B Cell Aplasia
Probability of B cell aplasia
1.00
0.75
0.50
0.25
0.00
Low tumor burden patients
High tumor burden patients
P = 0.76
0
0.5
1
1.5
Years since onset of remission
Number at risk
Strata
High 34 11 7 6 5
Low 90 49 39 35 24
Overall 124 60 46 41 29
0
0.5
1
1.5
Years since onset of remission
E
****
****
ns
Costimulatory molecule module score
0.15
0.10
0.05
0.00
B cell (likely healthy)
B cell (likely malignant)
DC
HEALTHY
DIAGNOSIS
REMISSION
RELAPSE

Fig 2

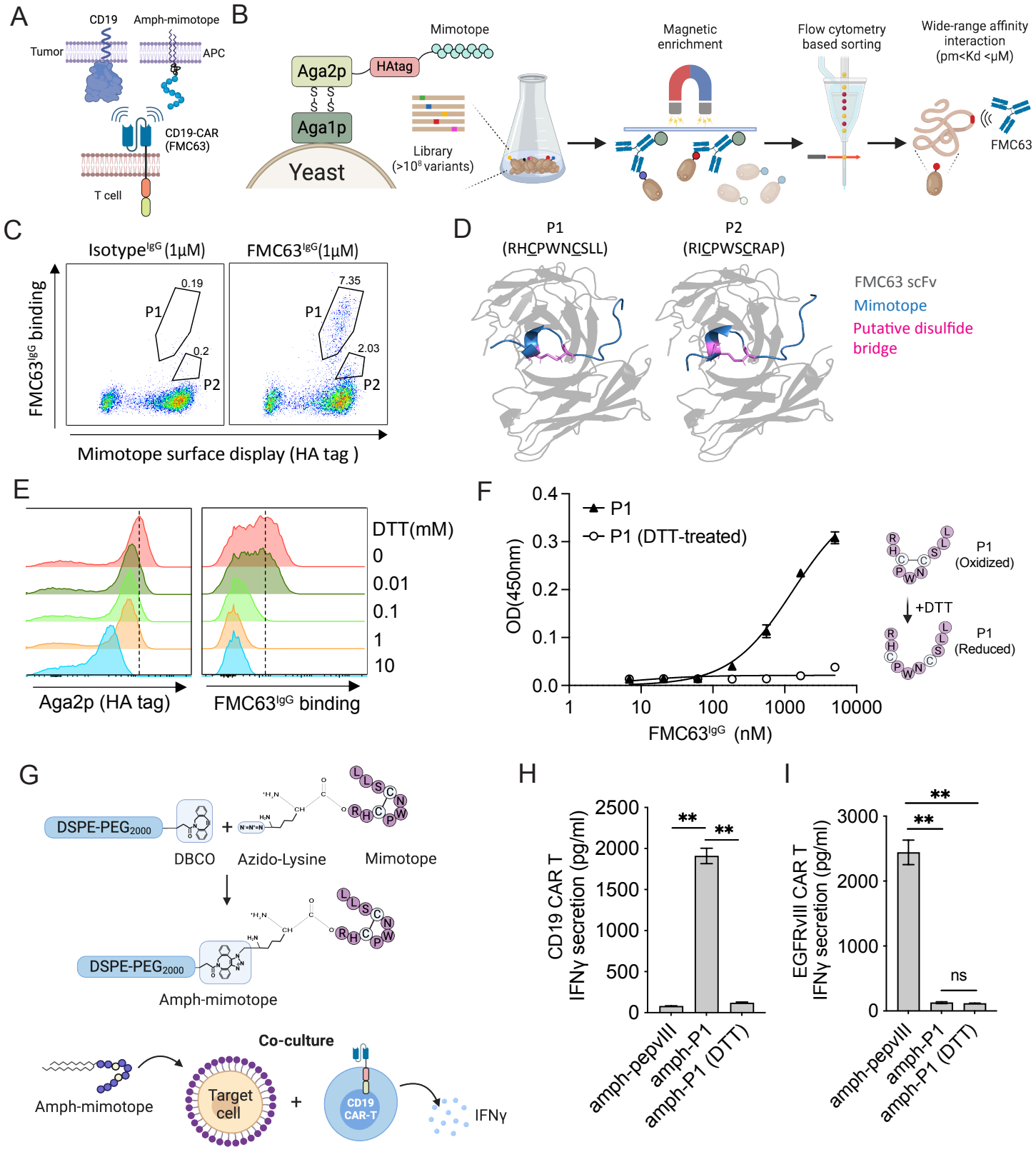
A
CD19
Amph-mimotope
Tumor
APC
CD19-CAR (FMC63)
T cell
B
Mimotope
Aga2p
HAtag
Aga1p
Yeast
Library (>10⁸ variants)
Magnetic enrichment
Flow cytometry based sorting
Wide-range affinity interaction (pm<Kd <μM)
FMC63
C
Isotype^IgG (1μM)
FMC63^IgG(1μM)
FMC63^IgG binding
P1
P2
0.19
0.2
7.35
2.03
Mimotope surface display (HA tag)
D
P1 (RHCPWNCSLL)
P2 (RICPWSCRAP)
FMC63 scFv
Mimotope
Putative disulfide bridge
E
DTT(mM)
0
0.01
0.1
1
10
Aga2p (HA tag)
FMC63^IgG binding
F
P1
P1 (DTT-treated)
OD(450nm)
FMC63^IgG (nM)
P1 (Oxidized)
+DTT
P1 (Reduced)
G
DSPE-PEG2000
DBCO
Azido-Lysine
Mimotope
Amph-mimotope
Co-culture
Amph-mimotope
Target cell
CD19 CAR-T
IFNγ
H
CD19 CAR T IFNγ secretion (pg/ml)
amph-pepvIII
amph-P1
amph-P1 (DTT)
I
EGFRvIII CAR T IFNγ secretion (pg/ml)
ns

Fig 3

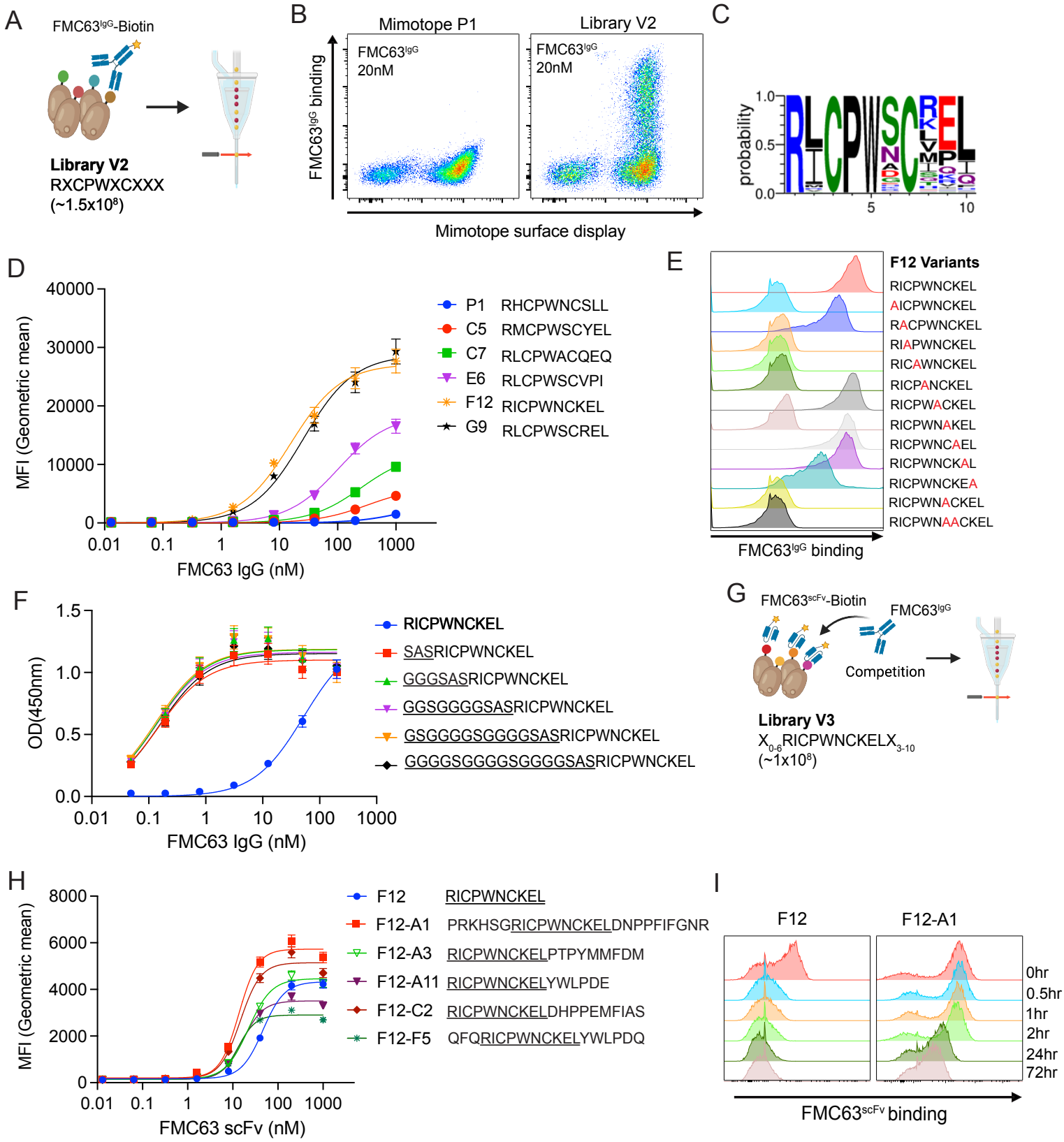
A
FMC63IgG-Biotin
Library V2
RXCPWXCXXX
(~1.5x10⁸)
B
Mimotope P1
Library V2
FMC63IgG
20nM
FMC63IgG binding
Mimotope surface display
C
probability
1.0
0.5
0.0
5
10
D
MFI (Geometric mean)
40000
30000
20000
10000
0
0.01
0.1
1
10
100
1000
FMC63 IgG (nM)
P1 RHCPWNCSLL
C5 RMCPWSCYEL
C7 RLCPWACQEQ
E6 RLCPWSCVPI
F12 RICPWNCKEL
G9 RLCPWSCREL
E
F12 Variants
RICPWNCKEL
AICPWNCKEL
RACPWNCKEL
RIAPWNCKEL
RICAWNCKEL
RICPANCKEL
RICPWACKEL
RICPWNAKEL
RICPWNCAEL
RICPWNCKAL
RICPWNCKEA
RICPWNACKEL
RICPWNAACKEL
FMC63IgG binding
F
OD(450nm)
1.5
1.0
0.5
0.0
0.01
0.1
1
10
100
1000
FMC63 IgG (nM)
RICPWNCKEL
SASRICPWNCKEL
GGGSASRICPWNCKEL
GGSGGGGSASRICPWNCKEL
GSGGGGSGGGGSASRICPWNCKEL
GGGGSGGGGSGGGGSASRICPWNCKEL
G
FMC63scFv-Biotin
FMC63IgG
Competition
Library V3
X0-6RICPWNCKELX3-10
(~1x10⁸)
H
MFI (Geometric mean)
8000
6000
4000
2000
0
0.01
0.1
1
10
100
1000
FMC63 scFv (nM)
F12 RICPWNCKEL
F12-A1 PRKHSGRICPWNCKELDNPPFIFGNR
F12-A3 RICPWNCKELPTPYMMFDM
F12-A11 RICPWNCKELYWLPDE
F12-C2 RICPWNCKELDHPPEMFIAS
F12-F5 QFQRICPWNCKELYWLPDQ
I
F12
F12-A1
0hr
0.5hr
1hr
2hr
24hr
72hr
FMC63scFv binding

Fig 4

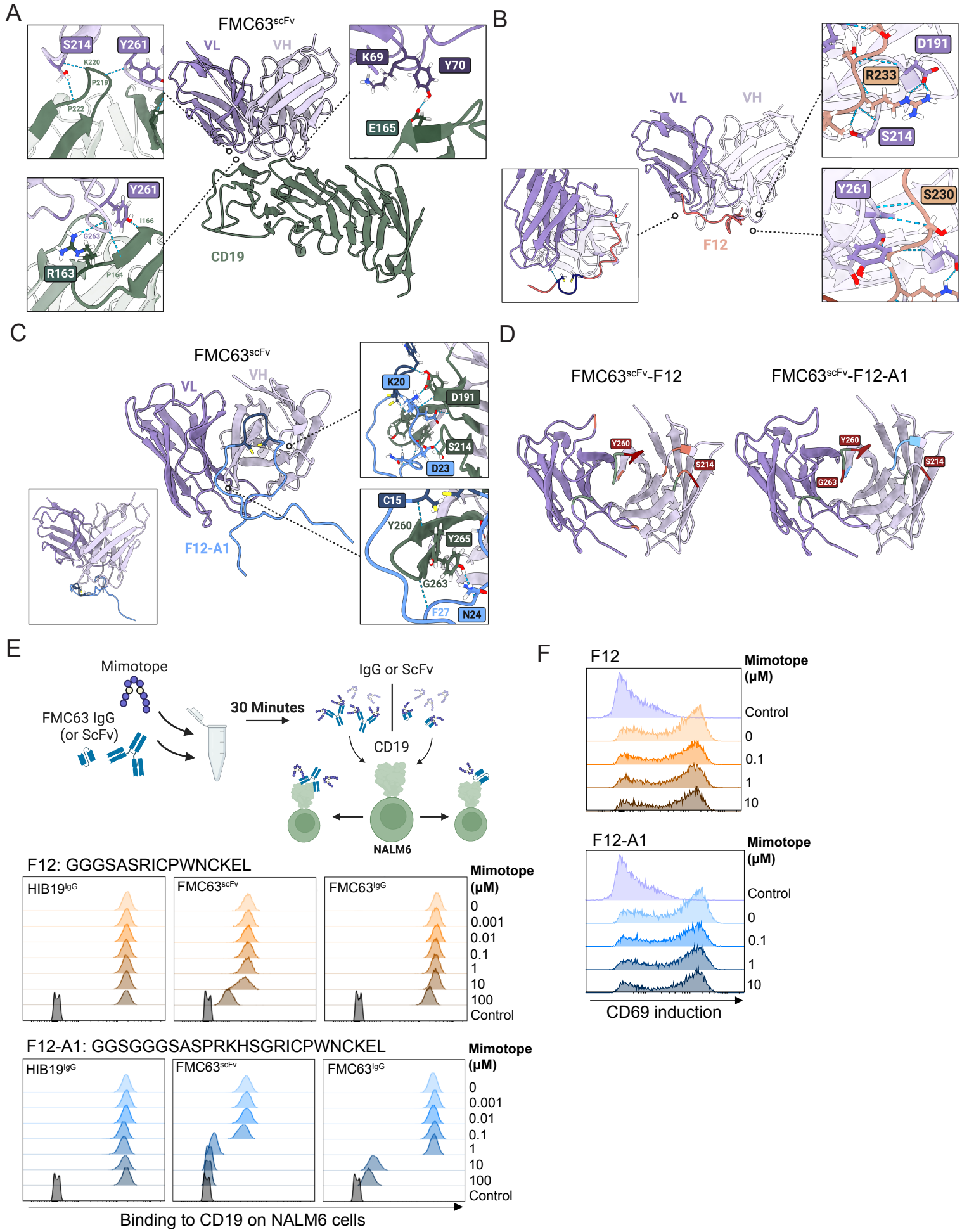
A
FMC63scFv
VL
VH
S214
Y261
K220
P219
P222
K69
Y70
E165
Y261
I166
G263
R163
P164
CD19
B
VL
VH
D191
R233
S214
Y261
S230
F12
C
FMC63scFv
VL
VH
K20
D191
S214
D23
F12-A1
C15
Y260
Y265
G263
F27
N24
D
FMC63scFv-F12
FMC63scFv-F12-A1
Y260
S214
Y260
G263
S214
E
Mimotope
FMC63 IgG
(or ScFv)
30 Minutes
IgG or ScFv
CD19
NALM6
F12: GGGSASRICPWNCKEL
HIB19IgG
FMC63scFv
FMC63IgG
Mimotope
(μM)
0
0.001
0.01
0.1
1
10
100
Control
F12-A1: GGSGGGSASPRKHSGRICPWNCKEL
HIB19IgG
FMC63scFv
FMC63IgG
Mimotope
(μM)
0
0.001
0.01
0.1
1
10
100
Control
Binding to CD19 on NALM6 cells
F
F12
Mimotope
(μM)
Control
0
0.1
1
10
F12-A1
Mimotope
(μM)
Control
0
0.1
1
10
CD69 induction

Fig 5

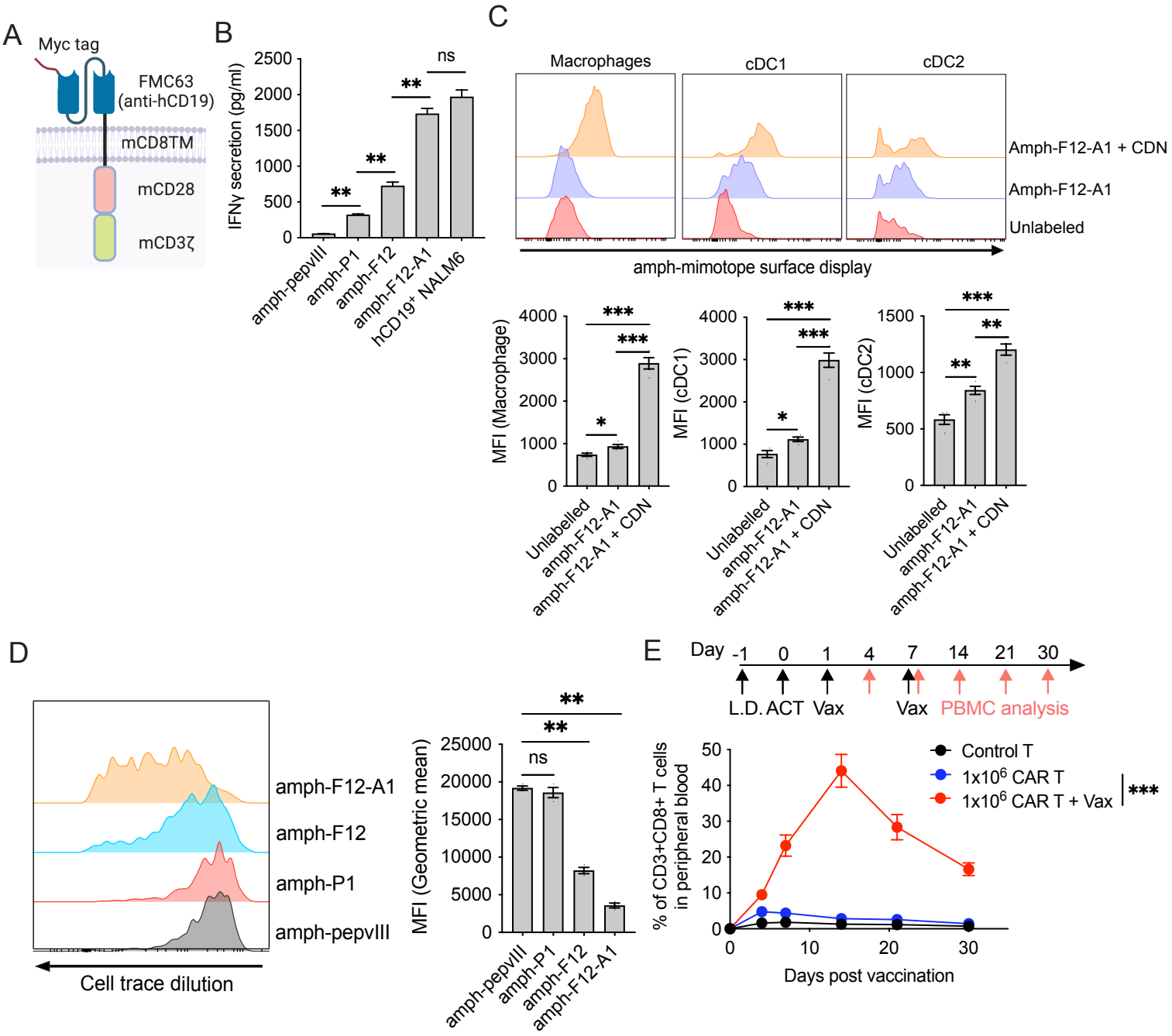
A
Myc tag
FMC63
(anti-hCD19)
mCD8TM
mCD28
mCD3ζ
B
IFNγ secretion (pg/ml)
2500
2000
1500
1000
500
0
**
**
**
ns
amph-pepvIII
amph-P1
amph-F12
amph-F12-A1
hCD19+ NALM6
C
Macrophages
cDC1
cDC2
Amph-F12-A1 + CDN
Amph-F12-A1
Unlabeled
amph-mimotope surface display
MFI (Macrophage)
MFI (cDC1)
MFI (cDC2)
4000
3000
2000
1000
0
1500
1000
500
***
***
*
**
Unlabelled
amph-F12-A1
amph-F12-A1 + CDN
D
amph-F12-A1
amph-F12
amph-P1
amph-pepvIII
Cell trace dilution
MFI (Geometric mean)
25000
20000
15000
10000
5000
0
**
**
ns
amph-pepvIII
amph-P1
amph-F12
amph-F12-A1
E
Day -1 0 1 4 7 14 21 30
L.D. ACT Vax
Vax PBMC analysis
% of CD3+CD8+ T cells in peripheral blood
50
40
30
20
10
0
Control T
1x10^6 CAR T
1x10^6 CAR T + Vax
***
0
10
20
30
Days post vaccination

Fig 6

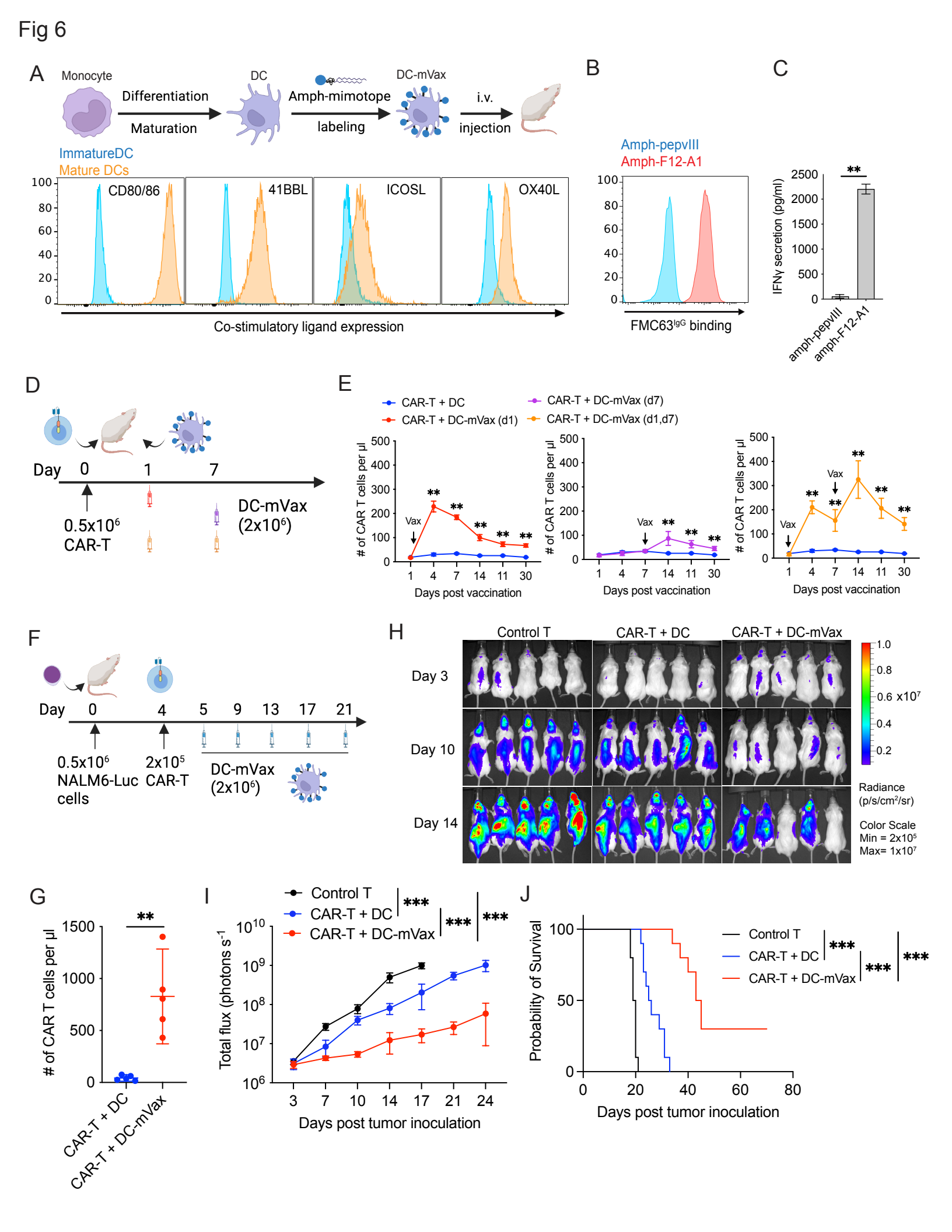
A
Monocyte
Differentiation
Maturation
DC
Amph-mimotope
labeling
DC-mVax
i.v.
injection
ImmatureDC
Mature DCs
CD80/86
41BBL
ICOSL
OX40L
Co-stimulatory ligand expression
B
Amph-pepvIII
Amph-F12-A1
FMC63IgG binding
C
IFNγ secretion (pg/ml)
amph-pepvIII
amph-F12-A1
D
Day 0 1 7
0.5x10⁶ CAR-T
DC-mVax (2x10⁶)
E
CAR-T + DC
CAR-T + DC-mVax (d1)
CAR-T + DC-mVax (d7)
CAR-T + DC-mVax (d1,d7)
# of CAR T cells per µl
Vax
Days post vaccination
F
Day 0 4 5 9 13 17 21
0.5x10⁶ NALM6-Luc cells
2x10⁵ CAR-T
DC-mVax (2x10⁶)
H
Control T
CAR-T + DC
CAR-T + DC-mVax
Day 3
Day 10
Day 14
Radiance (p/s/cm²/sr)
Color Scale
Min = 2x10⁵
Max= 1x10⁷
G
# of CAR T cells per µl
CAR-T + DC
CAR-T + DC-mVax
I
Control T
CAR-T + DC
CAR-T + DC-mVax
Total flux (photons s⁻¹)
Days post tumor inoculation
J
Probability of Survival
Control T
CAR-T + DC
CAR-T + DC-mVax
Days post tumor inoculation

MATERIALS AND METHODS

Clinical trial data

Pediatric *B-cell acute lymphoblastic leukemia*

Patient data from two studies of tisagenlecleucel for the treatment of CD19-positive relapsed or refractory B-acute lymphocytic leukemia (B-ALL) in children and young adults, NCT01626495 [1] (N=60 infused) and NCT02906371 (n=70 infused) [2] were pooled (n=130). In both studies, patients received lymphodepleting chemotherapy with fludarabine and cyclophosphamide followed by a pre-infusion bone marrow aspirate or biopsy to assess tumor burden, and infusion of tisagenlecleucel over 1-2 days. Patients were categorized based on the pre-infusion bone marrow aspirate or biopsy as high (≥40%, n=40) or low tumor burden (<40%, n=90). Peripherally circulating CD19 CAR-T cells were quantified by quantitative polymerase chain reaction (qPCR). Peripherally circulating normal B cells were quantified by flow cytometry. Data analyses were performed using R. The study protocols were approved by the institutional review boards of the Children's Hospital of Philadelphia and the University of Pennsylvania. Patients or their guardians provided written informed consent.

Adult B-cell acute lymphoblastic leukemia

We conducted a retrospective analysis of CAR T expansion in a cohort of adult B-ALL patients treated with the 4-1BB CART19 CTL019 (NCT02030847), now commercially known as tisagenlecleucel. Only patients with available pre-CART19 bone marrow involvement evaluation were included (n=29). Patients' characteristics were retrieved from the clinical trial database and electronic medical records as per an IRB-approved protocol. Tumor burden was defined as the percentage of bone marrow blast involvement before CAR T infusion. Patients with more than 5% of blasts were defined as high tumor burden (n=23), while patients with ≤5% blasts were considered low tumor burden (n=6). Peak of CAR T expansion was defined as the highest value of CAR19 copies/µg DNA after CAR T infusion, which typically occurs between days 7 and 14. CAR T cell expansion in the peripheral blood was evaluated using qPCR at multiple time points, as previously described[3,4]. A Student's t-test was used to compare CAR T peak. Significance was set at 0.05.

Adult B cell lymphoma

We conducted a retrospective analysis of CAR T expansion, according to tumor burden, in a cohort of B-cell Lymphoma patients treated with 4-1BB CART19 CTL019 (NCT02030834), now commercially known as tisagenlecleucel. Only patients with LDH levels available at CART19 infusion were included (n=37). Tumor burden was estimated per LDH serum levels at infusion day. Patients with LDH levels higher than 1.5-fold the upper normal limit were considered as high tumor burden (n=7). Peak of CAR T expansion was defined as the highest value of CAR19 copies/µg DNA after CAR T infusion, which typically occurs between days 7 and 14. CAR T cell expansion in the peripheral blood was evaluated using qPCR at multiple time points, as previously described[3,4]. Patients' characteristics were retrieved from the clinical trial database and electronic medical records as per IRB-approved protocols. A t-test was used to compare CAR T peak. Significance was set at 0.05.

Cell line and animals

K562, Jurkat, NALM6 and 293 phoenix cells were obtained from ATCC. The NALM6-Luc cell line was a gift from Dr. Michael Birnbaum at MIT. Wildtype female C57BL/6 mice (CD45.2$^+$), CD45.1$^+$ congenic mice, and NSG mice were purchased from the Jackson Laboratories. All animal studies were carried out following an IACUC-approved protocol following local, state, and federal guidelines. The EBY100 yeast strain was a gift from lab of K. Dane Wittrup at MIT.

Antibodies and recombinant proteins

FMC63 IgG, his-tagged FMC63 scFv, 1D3 IgG, anti-ALK IgG (ALK123) were cloned into the gWiz vector and used for recombinant protein production using Expi293 cells. Recombinant proteins were then purified using FPLC (Akta pure 25). Anti-hCD19 (HIB19) and anti-HA antibody were purchased from Biolegend. The anti-Myc antibody (9B11) was purchased from Cell Signaling.

Yeast mimotope library construction

We followed previously established protocols[5,6] to construct our yeast surface display libraries starting with the parental pCT-Con2 vector, except the following modifications that were tailored for the mimotope library: 1) The mimotope library PCR was carried out with nested PCRs. 1st PCR primers: Mimotope Lib F - AACTAGCAAAGGCAGCCCCATAAACAC and Mimotope Lib R- GATTTTGTTACATCTACACTGTTGTTATCAGATCTCGAGCTATTA<u>MNNMNNM NNMNNMNNMNNMNNMNNMNNMNNMNN</u>GCTAGCCGACCCTCCGCC. 2nd PCR primers: Min Cmyc EP F – GGCTCTGGTGGAGGCGGTAGCGGAGGCGGAGGGTCGGCTAGC and Min Cmyc EP R -GATTTTGTTACATCTACACTGTTGTTATCAGATCTCGAGCTATTA. PCR products were verified on a 2.5% agarose gel. The nested PCR products were extracted using the conventional pheno-chloroform and ethanol precipitation method, pelleted and dissolved in 15 µl H_2O. The parental pCT-Con2 vector (Addgene # 41843) was digested with NheI, SalI and XhoI, purified using gel extraction followed by a clean-up step using PCR clean-up columns and eluted in 20 µl H_2O. For electroporation, 4 µg digested backbone was pre-mixed with the entire PCR product with the maximum volume less than 20µl. Then, pre-chilled yeast cells were added to the DNA mixture before transferring to an electroporation cuvette.

To generate mimotope library V2 with a fixed motif (RXCPWXCXXX), the mimotope Lib R primer was replaced with mimotope Lib V2 R -GATTTTGTTACATCTACACTGTTGTTATCAGATCTCGA GCTATTA<u>MNNMNNMNNACAMNNCCACGGACAMNNACG</u> GCTAGCCGACCCTCCGCCTC. To generate mimotope library V3 with extended flanking sequences ($X_{0\text{-}6}$RICPWNCKEL$X_{3\text{-}10}$), mimotope Lib R primer was replaced with:

mimotope Lib V3 R1 - GATTTTGTTACATCTACACTGTTGTTATCAGATCTCGAGCTATTA <u>MNNMNNMNNAAGCTCCTTACAATTCCACGGACAAATACGMNNMNNMNN</u> GCTAGCCGACCCTCCGCCTC, to generate library X_3RICPWNCKELX_3.

mimotope Lib V3 R2 - GATTTTGTTACATCTACACTGTTGTTATCAGATCTCGAGCTATTA <u>AAGCTCCTTACAATTCCACGGACAAATACGMNNMNNMNNMNNMNNMNN</u> GCTAGCCGACCCTCCGCCTC, to generate library X_6RICPWNCKEL.

mimotope Lib V3 R3 - GATTTTGTTACATCTACACTGTTGTTATCAGATCTCGAGCTATTA <u>MNNMNNMNNMNNMNNMNNAAGCTCCTTACAATTCCACGGACAAATACG</u> GCTAGCCGACCCTCCGCCTC, to generate library XRICPWNCKELX_6.

mimotope Lib V3 R4 - GATTTTGTTACATCTACACTGTTGTTATCAGATCTCGAGCTATTA <u>MNNMNNMNNAAGCTCCTTACAATTCCACGGACAAATACGMNNMNNMNNMNNMNNMNN</u> GCTAGCCGACCCTCCGCCTC, to generate library X_6RICPWNCKELX_3.

mimotope Lib V3 R5 - GATTTTGTTACATCTACACTGTTGTTATCAGATCTCGAGCTATTA <u>MNNMNNMNNMNNMNNMNNAAGCTCCTTACAATTCCACGGACAAATACGMNNMNNMNN</u> GCTAGCCGACCCTCCGCCTC, to generate library X_3RICPWNCKELX_6.

mimotope Lib V3 R6 - GATTTTGTTACATCTACACTGTTGTTATCAGATCTCGAGCTATTA <u>MNNMNNMNNMNNMNNMNNMNNMNNMNNMNNAAGCTCCTTACAATTCCACGGACAAATAC G</u>GCTAGCCGACCCTCCGCCTC, to generate library RICPWNCKELX_{10}.

mimotope Lib V3 R7 - GATTTTGTTACATCTACACTGTTGTTATCAGATCTCGAGCTATTA <u>AAGCTCCTTACAATTCCACGGACAAATACGMNNMNNMNNMNNMNNMNNMNNMNNMNNMNNMN N</u>GCTAGCCGACCCTCCGCCTC, to generate library X_{10}RICPWNCKEL. A 10x diversity

(definition of diversity: total number of mimotope variants within the yeast library) of all individual V3 libraries were mixed to create the final X_{0-6}RICPWNCKELX$_{3-10}$ library.

Yeast surface display screen

To prepare biotinylated recombinant protein, 200 µl of antibody or scFv at 1 mg/ml in PBS was mixed with 10% volume of 1M sodium bicarbonate to adjust pH to 7-8 followed by addition of EZ-Link sulfo-NHS-LC-Biotin (ThermoFisher) to reach a 5:1 biotin:protein molar ratio. The mixture was stirred at room temperature for 1 hour, followed by spin-column purification and subsequent quantification using nanodrop.

The yeast library was thawed, passaged and prepared as previously described[5,6]. To prepare for the screen, yeast cells were grown in SD-CAA until the OD600 reached 6-8. 30x diversity (or at least 100M) yeast cells were transferred into SG-CAA medium supplemented with 5% SD-CAA. Yeast were shaken at 20°C overnight to induce protein display on the cell surfaces. We noticed that 5% of SD-CAA improved mimotope display on the yeast cell surface, and usually >75% induction could be achieved.

The yeast library screen was performed as previously described[5,6] with the following modifications: 1) 15x diversity was used per sort (7.5e9 for the mimotope library). Yeast was spun down at 3500RPM for 5 minutes, washed in cold 1x PBSA (1x PBS + 0.1% BSA), then aliquoted into 2 x 2 mL tubes (3.75e9 per tube). Yeast were then spun at 12,000xg for 1 minute and resuspended in 1mL 1x PBSA. 2) For positive-sort beads (Dynabeads™ Biotin Binder [ThermoFisher] pre-coated with 6.7-33pmoles of biotinylated IgG or scFv as previous described[6]), non-bound yeast was gently removed, and the remaining beads were washed to remove unbound or weakly bound yeast cells with 1ml 1x PBSA by inverting repeatedly. Supernatant was removed, then yeast were resuspended in 1 mL SD-CAA, and counted to determine diversity. 3) 10x diversity of 1st round positive-sorted yeast was pelleted at 12,000xg for 1 minute. Yeast were inoculated into premade 5 ml SG-CAA with 5% SD-CAA, then induced at 20°C overnight (at least 8 hr is needed for reasonable induction). At least 20x diversity was pelleted and washed once with 1x PBSA, then resuspended in 1ml 1x PBSA. 4) For the 2nd round of magnetic enrichment, the first bare bead sort and two subsequent negative sorts using beads coated with isotype control IgG were carried out at 0.5 beads per yeast cell for >=2 hours at 4°C. This step was critical to remove background and non-specific binders. The final positive sort using FMC63$_{IgG}$-coated beads was carried out following the standard enrichment procedure but with longer washes (30 sec) to improve stringency. Enriched yeast were counted under microscopy to determine the diversity. At this point, the diversity should have been massively reduced. 5) 30x of enriched and induced yeast cells from the 2nd round of positive sorting were pelleted, stained with 30 µl 5 µM control IgG or FMC63 IgG at 4°C for 30 minutes. Yeast were washed twice with 1 ml of 1x PBSA to remove residual antibody. When a plate was used for staining, yeast were washed 3-4 times with 200 µl. The pellet was stained in 50 µl of 1:100 dilution PE-Streptavidin and BV421-HA for 20 minutes on ice. Yeast were washed twice with 1 ml of 1x PBSA prior to flow cytometry sorting (BD FACS Aria), with adjustments made as previously described for using a plate when needed. The top 0.5-1% of the major population based on FMC63 IgG binding was sorted. Usually following this modified protocol, a clearly distinct yeast population could be observed during flow cytometry analysis. 6) FMC63 IgG was used at 0.5µM for the subsequent flow cytometry-based sort. We alternated between streptavidin and anti-biotin antibodies when staining yeast populations for flow cytometry to avoid selecting streptavidin binders. 7) For kinetic sorting, 10x of the library V3 was stained with 50nM biotinylated FMC63 scFv for 30min, washed 2x with 1x PBS and then incubated with 500 nM of non-modified FMC63 IgG for 1 hour or overnight.

Plasmid extraction from yeast cells and sanger sequencing

The Zymo yeast DNA extraction kit was used with a modified protocol. Briefly, 50 million yeast cells were pelleted and resuspended in 200 µl solution I. 3 µl of zymolyase was added, then the mixture was vortexed and incubated at 37°C for 1 hour. 200 µl of solution 2 was added, then mixed gently by flipping tubes upside down a few times, and leaving at room temperature for 5 min. 400 µl of solution 3 was added, then mixed well by shaking. The mixture was spun at top speed for 5 minutes. Supernatant was transferred to a new 1.5 ml EP tube and spun at top speed for 5 minutes to remove all white clumps. The clear lysate was transferred onto a spin column from a regular miniprep kit instead of the column provided in the Zymo yeast DNA extraction kit, then spun at 11,000g for 30 seconds. Columns were washed with 600 µl of wash buffer from the miniprep kit, spun again at 11,000g for 1 minute to dry the membrane, and then eluted with 50 µl of H_2O. Eluted DNA was cleaned using a PCR clean-up kit (Invitrogen) following the manufacturer's protocol. DNA was eluted in 20 µl H_2O and quantified using nanodrop. 5 µl of clean DNA was transformed into 50 µl of DH5α commercial competent cells (NEB). The whole transformation was spread onto a 10 cm ampicillin agar plate. Individual bacteria colonies were picked and inoculated onto a 96-well agar plate and grown overnight. The entire plate was sent for miniprep and sanger sequencing.

ELISA

Mouse and human ELISA assays were performed following the manufacturer's protocol (Mouse and human IFN-γ Duo set, R&D systems). For ELISA monitoring of FMC63 IgG binding to mimotopes, mimotope was dissolved in 1x PBS and coated onto a 96-well maxisorp plate at 4 µg/ml, 50 µl per well, sealed and kept at 25°C overnight. The next day, the plate was washed 4x followed by 1hr blocking (1% BSA in 1x PBS) at 25°C. After washing, FMC63 IgG was diluted to desired concentration in the blocking buffer and added to each well at 50 µl per well. After 1hr incubation at 25°C, plates were washed again, substrate was added and the remainder of the assay was performed as previously described[7].

Construction of murine and human CARs

Murine CAR-expressing constructs were generated by fusing geneblock fragments (custom ordered from IDT) into an MSCV retroviral vector. The hybrid FMC63-mCAR sequence is composed of a mouse CD8 signal peptide, FMC63 scFv, mouse CD8a hinge and transmembrane domain, CD28 costimulatory domain and CD3ζ intracellular domain as described in our previous work[7]. Human CAR-expressing constructs were generated by fusing geneblock fragments (custom ordered from IDT) into a lentiviral vector containing the EF1a promoter. The CD19-CAR is composed of a human CD8 signal peptide, FMC63 scFv (VLVH), human CD8 hinge and transmembrane domain, CD28 costimulatory domain and CD3ζ intracellular domain as described previously[7] . To facilitate CAR detection by flow cytometry, a Myc tag was inserted at the N-terminus of FMC63 scFv immediately following the signal peptide in both constructs.

Virus production

For optimal retrovirus production, 293 phoenix cells were cultured till 80% confluence, then split at 1:2 for further expansion. 24 hr later, 5.6×10^6 cells were seeded in a 10 cm dish and cultured for 16 hr till the confluency reached 70%. 30 min – 1 hr before transfection, each 10 cm dish was replenished with 10 ml pre-warmed medium. Transfection was carried out using the calcium phosphate method following the manufacturer's protocol (Clontech). Briefly, for each transfection, 18µg of plasmid (16.2 µg of CAR plasmid plus 1.8 µg of Eco packaging plasmid) was added to 610 µl of ddH_2O, followed by addition of 87µl of 2 M $CaCl_2$. 700µl of 2x HBS was then added in a dropwise manner with gentle vortexing. After a 10 min incubation at 25°C, the transfection mixture was gently added to phoenix cells. After 30 min incubation at 37°C, the plate was checked for the

202 formation of fine particles, as a sign of successful transfection. The next day, old medium was
203 removed and replenished with 8 ml of pre-warmed medium without disturbing the cells. Virus-
204 containing supernatant was collected 36 hr later and passed through a 0.45 um filter to remove
205 cell debris, designated as the "24hr" batch. Dishes were refilled with 10 ml of fresh medium and
206 cultured for another 24 hr to collect viruses again, designated as the "48hr" batch, this process
207 can be repeated for another two days to collect a "72hr" batch and "96hr" batch. All virus
208 supernatant was aliquoted and stored at -80°C. Virus transduction rate was evaluated in a 12-
209 well format by mixing 0.5 million activated T cells with 0.5ml of viruses from each batch. Plate
210 coating, spin infection and flow cytometry analysis of CAR expression were carried out as
211 described above. In the majority of experiments, the "48hr" and "72hr" batches yielded viruses
212 that transduced T cells at 90-95% efficiency, the "24hr" and "96hr" batch viruses led to >80%
213 transduction. Only viruses with >80% transduction rate were used for animal studies. Lentivirus
214 was produced as previously described[8].
215
216 **Primary mouse T cell isolation and CAR T cell production**
217 For T cell activation, 6-well plates were pre-coated with 5 ml of anti-CD3 (0.5 μg/ml, Clone: 2C11)
218 and anti-CD28 (5 μg/ml, Clone: 37.51) per well at 4°C for 18 hr. $CD8^+$ T cells were isolated using
219 a negative selection kit (Stem Cell Technology), and seeded onto pre-coated 6-well plates at 5
220 $x10^6$ cells/well in 5 ml of complete medium (RPMI + penicillin/streptomycin + 10% FBS + 1x NEAA
221 + 1x Sodium pyruvate + 1x 2-mercaptoethanol + 1x ITS [Insulin-Transferrin-Selenium,
222 ThermoFisher]). Cells were cultured at 37°C for 48 hr without disturbance. 24 hr before
223 transduction, non-TC treated plates were coated with 15 μg/ml of retronectin (Clontech). On day
224 2, cells were collected, counted and resuspended at $2x10^6$ cells/ml in complete medium
225 supplemented with 20 μg/ml of polybrene and 40 IU/mL of mIL-2. Retronectin-coated plates were
226 blocked with 0.05% FBS containing PBS for 30 min before use. 1 ml of virus supernatant was first
227 added into each well of the blocked retronectin plate, then 1 mL of the above cell suspension was
228 added and mixed well by gentle shaking to reach the working concentration of polybrene at 10
229 μg/ml and mIL-2 at 20 IU/ml. Spin infection was carried out at 2000x*g* for 120 min at 32°C. Plates
230 were then carefully transferred to an incubator and maintained overnight. On day 3, plates were
231 briefly centrifuged at 1,000x*g* for 1 min, and virus-containing supernatants were carefully removed.
232 3 mL of fresh complete medium containing 20 IU/ml of mIL-2 were then added into each well.
233 Cells were passaged 1:2 every 12 hr with fresh complete medium containing 20 IU/mL of mIL-2.
234 Transduction efficiency was evaluated by surface staining of a c-Myc tag included in the CAR
235 construct[7] using an anti-Myc antibody (Cell signaling, Clone:9B11) ~30 hr after transduction. If
236 needed, on day 3, after flow cytometry analysis of virus transduction, CAR T cells could be frozen
237 down and stored for assays at a later time. For in vivo experiments, CAR T cells were used on
238 day 4. For *in vitro* experiments, CAR T cells were cultured until day 5.
239
240 **Primary human T cell isolation and CAR T cell production**
241 Buffy coats were obtained from anonymous healthy donors (Research Blood Components, LLC,
242 Boston, MA, USA). Total peripheral blood mononuclear cells (PBMCs) were isolated by Ficoll-
243 Paque PLUS gradient separation. $CD8^+$T cells were isolated directly using the EasySep Human
244 $CD8^+$ T cell isolation kit (Stemcell). T cells were activated with Human T-Activator CD3/CD28
245 Dynabeads (ThermoFisher) at a bead-to-cell ratio of 3:1 in complete medium supplemented with
246 30 IU/mL recombinant human IL-2 (PeproTech). After two days of activation, T cells were
247 transduced with lentiviral supernatants as described above for murine T cells, and transduction
248 efficiencies were determined by flow cytometry 2 days later. If transduction efficiency was less
249 than 50%, CAR^+ T cells were enriched by staining total expanded T cells with a PE-conjugated
250 anti-Myc antibody followed by staining with anti-PE microbeads and magnetic selection for CAR^+

T cells. Enriched CAR T cells were continuously expanded till day 7 for adoptive transfer to NSG mice.

Mimotope, amphiphile-mimotope production and vaccination

Various mimotopes were custom synthesized (GenScript). The mimotope with a thioacetal bond was synthesized according to a previously published protocol[9] and verified by MALDI. Amph-mimotope molecules were produced and purified as previously described with modifications as indicated below[7]. Briefly, mimotope peptides (with an N-terminal Azido lysine) were dissolved in H_2O at 10 mg/mL and mixed with 1.1 molar equivalent of DSPE-PEG2k-DBCO (Avanti). The mixture was agitated at 25°C for 24 hr. Conjugation efficiency was analyzed using a C4 column on HPLC (Schimadzu). Typically, the conjugation efficiency reached >95%. When the conjugation efficiency was low, unconjugated peptide was removed using HPLC and the conjugates were collected. The resulting products were lyophilized, re-dissolved in PBS, quantified using nanodrop and stored at -20°C. For vaccination, unless otherwise stated, mice received weekly s.c. injection of 10 μg peptide equivalent of amph-mimotope mixed with 25 μg of Cyclic-di-GMP (CDG, Invivogen) in 100μl 1x PBS, administered 50 μl to each side at the tail base.

***In vitro* and *in vivo* amph-mimotope labeling**

For *in vitro* labeling, target cells were pelleted at 1,000x*g* for 3min and washed with PBS twice to remove residual protein. The cell pellet was then resuspended at $1x10^6$ cells/ml in PBS containing amph-mimotope molecules at the indicated concentrations and incubated at 37°C for 30 min. The labeling reaction was stopped by pelleting cells and washing with PBS twice. For *in vivo* labeling, mice received 10μg peptide equivalent of amph-mimotope with or without CDG as described above. 24 hr later, Inguinal LNs were extracted and dissociated into single cell suspension for flow cytometry staining for macrophages ($MHCII^+CD11b^+CD11c^-F4/80^+$), cDC1($MHCII^+CD11c^+CD11b^{low/-}CD24^+$) and cDC2 ($MHCII^+CD11c^+CD11b^+CD24^{low/-}$) as previously described[10]. To detect amph-mimotope decoration of various lymph node cell populations, 100nM of biotinylated FMC63 IgG was included in the antibody cocktail followed by secondary staining with Alex 647-streptavidin.

CAR T functionality assay

The functionality of CAR-T cells was assessed by co-coculturing with target cells *in vitro*. 96-well U bottom plates were used. Unless otherwise stated, $1x10^5$ sorted CAR T cells or unsorted CAR-T cells (>70% CAR T cells) possessing an equivalent number of CAR+ T cells were mixed with $1x10^4$ target cells in a total volume of 200μl complete medium containing 20IU/ml of mIL-2 (for mouse hybrid CAR T) or 30IU/ml of hIL-2 (for human CAR T). After 6 hr co-culture, cells were pelleted at 2,000x*g* for 5 min, and supernatants were harvested for IFN-γ ELISA.

Modeling mimotope interaction with FMC63

Both F12 and F12-A1 were modeled as multimers using Alphafold with default settings[11]. Alphafold generated 25 structures that were relaxed using the AMBER force field option, then ranked internally. All 25 structures were clustered with Rosetta[12] using an RMSD cut-off of 2.0Å to better understand which conformations were favored during modeling. For both F12 and F12-A1, the top ranked model resided in the cluster with the most members, and the most favorable energy when scored using the Rosetta score function[13,14]. The top ranked structure was minimized using the Rosetta FastRelax[15] protocol with deviations up to 3.0Å allowed, to eliminate any clashes between sidechains and achieve a more favorable conformation when scored using Ref2015. FastRelax produced 100 constructs, of which the construct with the most favorable energy was designated as the candidate structure. PDB 7URV was similarly minimized, with deviations up to 0.5Å allowed, to ensure coordinates are constrained to the crystal structure. All interfaces were analyzed using the PDBePISA webserver[16].

302
303 ***In vivo* tracking of CAR-T proliferation and response to amph-mimotope stimulation in**
304 **syngeneic mouse**
305 To monitor short-term amph-mimotope stimulation of CAR-T cells *in vivo*, $2x10^6$ murine hybrid
306 FMC63-mCAR T cells and untransduced T cells were mixed at a 1:1 ratio and labeled with 2.5
307 μM CTV and i.v. infused into recipient C57BL/6 mice. 16 hr later, 100 μl of amph-mimotope
308 vaccine (10 nmol of amph-mimotope mixed with 25μg CDG in 100μl PBS) was s.c. injected into
309 recipient mice, with 50 μl on each side of the tail base. After an additional 48 hr, mice were
310 euthanized and inguinal LNs were excised for flow cytometry analysis. Live $CD3^+CD8^+CTV^+$ cells
311 were gated as donor cells, and staining for the Myc tag on the CAR was used to distinguish CAR-
312 T cells from non-CAR-T cells. For long-term monitoring of hybrid FMC63-mCAR T cell expansion
313 in response to amph-mimotope vaccination, recipient CD45.2 mice received sublethal
314 lymphodepletion (500cGy gamma irradiation) on day -1 followed by i.v. infusion of $1x10^6$ CD45.1
315 FMC63-mCAR T cells on day 0. Two weekly doses of amph-mimotope vaccines were given on
316 day 1 and day 7, peripheral blood was sampled on day 4, day 7 and then every week thereafter
317 for enumeration of CAR T cells.
318
319 **Preparation of monocyte-derived DCs and amph-mimotope labeling**
320 Peripheral blood mononuclear cells were isolated from a buffy coat using Ficoll-Paque density
321 gradient. $CD14^+$ monocytes were then purified using the pan monocyte isolation kit (Miltenyi
322 BioTec). The characterization and differentiation of monocyte to immature DCs were performed
323 as previously described[17]. DC maturation was carried out using LPS and IFN-γ as reported
324 previously[18]. To label mature DC for *in vivo* vaccination, mature DCs were washed with 1x PBS
325 twice and then stained with 500 nM of amph-mimotope.
326
327 **B-ALL mouse model and therapeutic studies**
328 All animal work was conducted under an MIT Division of Comparative Medicine institute animal
329 care, used a committee-approved animal protocol by the Committee of Animal Care at MIT, and
330 used a committee-approved protocol in accordance with federal, state, and local guidelines. 8-12
331 week-old NOD.Cg-PrkdcscidIL2rgtm- 1Wjl/SzJ (NSG) mice (Jackson Laboratory) were injected
332 with $0.5x10^6$ NALM6-Luc cells and randomly assigned into each treatment group. On day 4,
333 leukemia bearing NSG mice received either mock treatment or a suboptimal dose of CD19 CAR
334 T cells ($2x10^5$) intravenously. 24 hours later, one group of CAR T-treated mice also received amph-
335 mimotope decorated MoDCs (DC-mVax) every four days. Leukemia progression was
336 subsequently monitored every 4-7 days using a Xenogen IVIS fluorescence/bioluminescence
337 imaging system (PerkinElmer) with intraperitoneal administration of 150mg kg−1 d-luciferin K+
338 salt (PerkinElmer 122799). Total photon counts or radiance were quantified using Living image
339 4.5. Mice were monitored daily and euthanized at morbidity, >20% weight loss, severe graft versus
340 host disease, or as recommended by the veterinarian. To monitor CAR T cell expansion and
341 persistence, peripheral blood was collected retro-orbitally, 50μl from each mouse were used for
342 each flow cytometry analysis. Red blood cells were lysed in ACK Lysis Buffer (Thermo
343 Fisher) prior to flow cytometry staining and the total number of PBMCs per microliter blood in
344 each sample was estimated by cell counting under microscope.
345
346 **Data mining and bioinformatic analysis**
347 Single-cell RNA-sequencing data from bone marrow of human patients with acute lymphoblastic
348 leukemia was obtained from GSE134759. Cells with under 500 unique genes detected were
349 filtered, and the data was normalized by library size using the “NormalizeData” function in Seurat.
350 Variable features were selected using the “FindVariableFeatures” function, followed by data
351 scaling with the “ScaleData” function and principal components analysis using “RunPCA”. The
352 data was processed for batch correction using Harmony. Clusters were defined using the

"FindClusters" function, and two-dimensional embeddings were generated using uniform manifold approximation and projection (UMAP). Differential gene expression analysis was performed using the "FindMarkers" function. Likely-malignant B cells were identified as two clusters of B cells that were primarily detected in samples with a diagnosis of "Diagnosis" or "Relapse". A score for costimulatory marker expression was computed using the "AddModuleScore" function in Seurat with the following list of genes: *CD80, CD86, TNFSF9, ICOSLG, TNFSF4, TNFSF18, TNFSF14.*

Statistics, selection of animals and justification of sample size

Statistical analyses were performed using GraphPad Prism 8. Animal survival was analyzed using log-rank (Mantel-Cox) test. All pair-wise comparisons were analyzed by student's t-test. Multi-group comparisons were carried out using a one-way ANOVA with Tukey's multiple comparisons test. Experiments that involved repeated measures over a time course, such as the total flux, were analyzed using a RM (repeated measures) two-way ANOVA based on a general linear model (GLM). The RM design included factors for time, treatment and their interaction. Tukey's multiple comparisons test was carried out for the main treatment effect. P-values are adjusted to account for multiple comparisons in both one-way ANOVA, and RM two-way ANOVA. We determined the size of samples for experiments involving either quantitative or qualitative data as previously reported[20]. Based on our previous experience with the animal models and as reported by others[21–23], we consider the therapy as significant if it increases the survival of animals up to 100% within 4 weeks, and >=5 animals per group is necessary to achieve this goal with 95% confidence interval and at 80% power.

EXTENDED DATA FIGURES

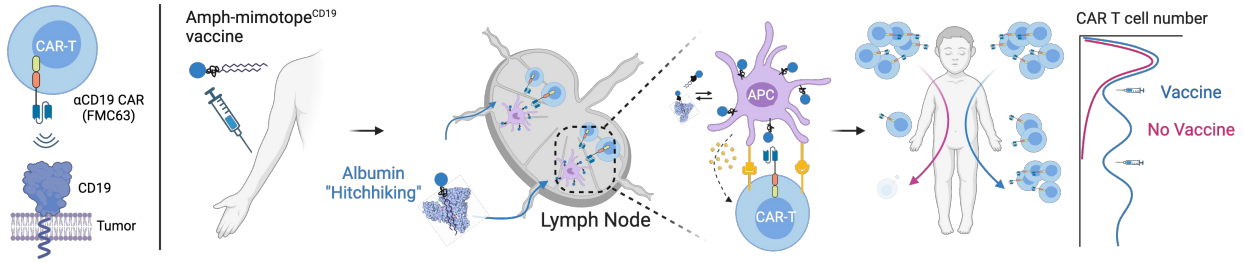

Figure 1: The concept of designing an amph-mimotope vaccine for CD19-CAR T cell therapy.

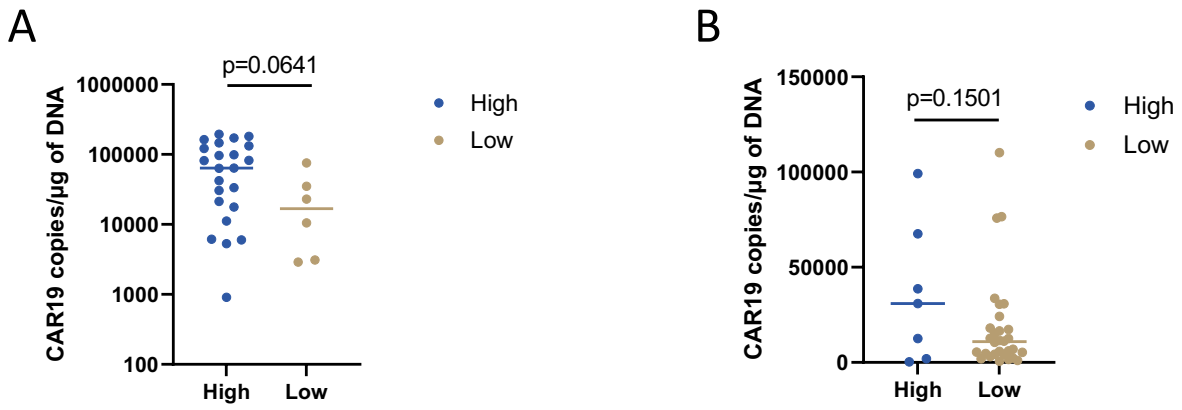

Extended Data Figure 2. CD19 CAR-T cell expansion in Adult B-ALL and B-cell lymphoma patients with initial high or low tumor burden. (**A**) The impact of high tumor burden on CART expansion in a cohort of relapsed/refractory ALL patients (n=29) treated with 4-1BB CART19 (CTL019; NCT02030847). High tumor burden was defined as bone marrow involvement before CART19 higher than 5%. The majority of patients (23/29, 79.3%) had a high disease burden before treatment. High tumor burden correlated with higher peak of expansion (CAR19 copies/µg of DNA: high tumor burden: 77,109 vs. low tumor burden: 25,064; p=0.0641;). (**B**) The impact of high tumor burden on CART expansion in a cohort of relapsed/refractory B-NHL patients treated with 4-1BB CART19 CTL019 within a clinical trial (n=37; NCT02030834). High tumor burden was defined as serum LDH higher than 1.5 folds the upper normal limit at infusion. In this cohort, we observed a trend toward higher CART19 expansion in patients with high disease burden (n=7, 18.9%) than in patients with low tumor burden (n=30, 81.1%) (CAR19 copies/µg of DNA 35,857 vs 18,718 respectively; p=0.1501).

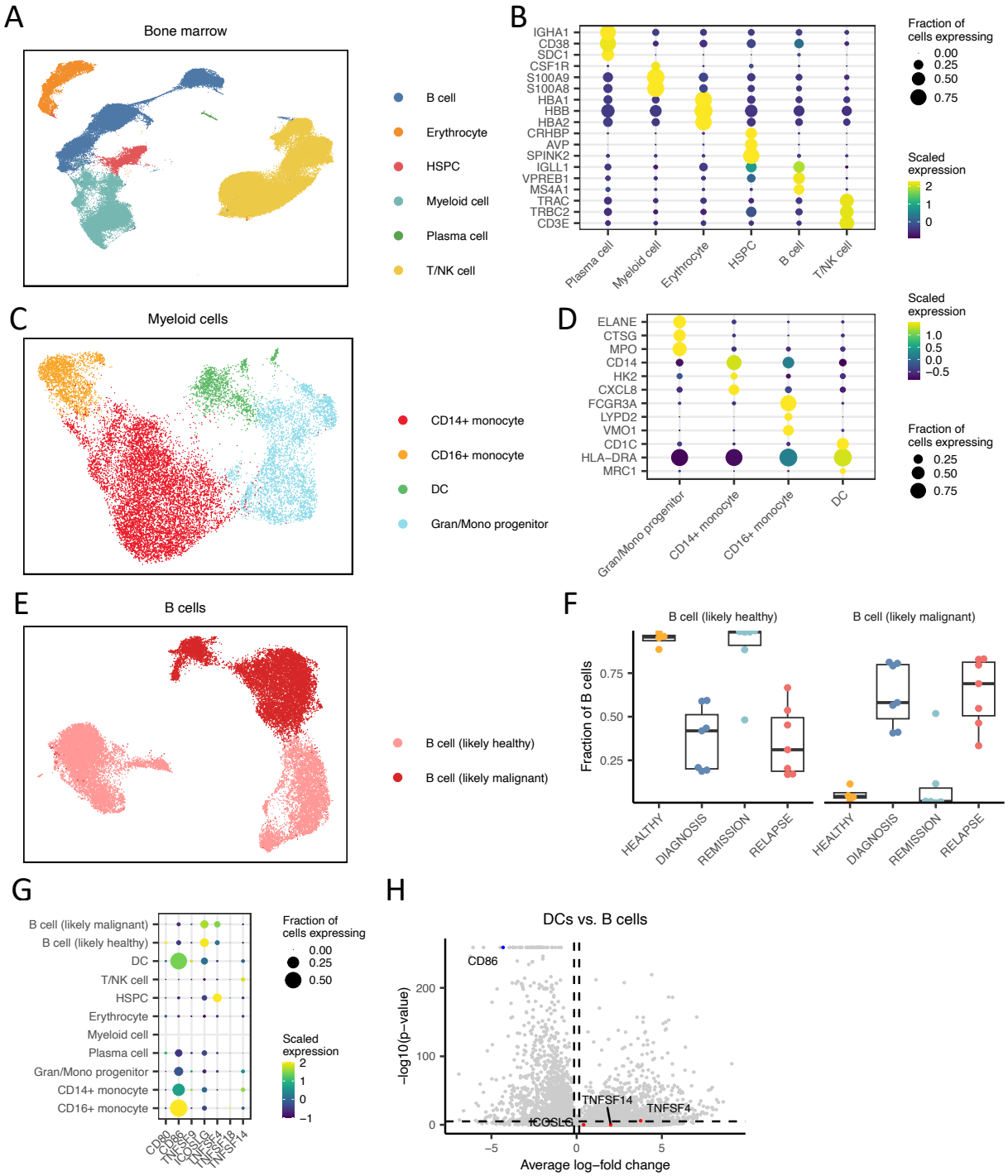
A
Bone marrow
B cell
Erythrocyte
HSPC
Myeloid cell
Plasma cell
T/NK cell
B
IGHA1
CD38
SDC1
CSF1R
S100A9
S100A8
HBA1
HBB
HBA2
CRHBP
AVP
SPINK2
IGLL1
VPREB1
MS4A1
TRAC
TRBC2
CD3E
Plasma cell
Myeloid cell
Erythrocyte
HSPC
B cell
T/NK cell
Fraction of cells expressing
0.00
0.25
0.50
0.75
Scaled expression
2
1
0
C
Myeloid cells
CD14+ monocyte
CD16+ monocyte
DC
Gran/Mono progenitor
D
ELANE
CTSG
MPO
CD14
HK2
CXCL8
FCGR3A
LYPD2
VMO1
CD1C
HLA–DRA
MRC1
Gran/Mono progenitor
CD14+ monocyte
CD16+ monocyte
DC
Scaled expression
1.0
0.5
0.0
−0.5
Fraction of cells expressing
0.25
0.50
0.75
E
B cells
B cell (likely healthy)
B cell (likely malignant)
F
B cell (likely healthy)
B cell (likely malignant)
Fraction of B cells
0.75
0.50
0.25
HEALTHY
DIAGNOSIS
REMISSION
RELAPSE
HEALTHY
DIAGNOSIS
REMISSION
RELAPSE
G
B cell (likely malignant)
B cell (likely healthy)
DC
T/NK cell
HSPC
Erythrocyte
Myeloid cell
Plasma cell
Gran/Mono progenitor
CD14+ monocyte
CD16+ monocyte
CD80
CD86
TNFSF9
ICOSLG
TNFSF4
TNFSF18
TNFSF14
Fraction of cells expressing
0.00
0.25
0.50
Scaled expression
2
1
0
−1
H
DCs vs. B cells
CD86
TNFSF14
TNFSF4
ICOSLG
−log10(p−value)
200
100
0
−5
0
5
Average log−fold change

Extended Data Figure 3. Single cell RNA-seq analysis of immune cells from B-ALL patients. **A**) UMAP of single cells isolated from the bone marrow of human AML patients, colored by cell phenotype. **B**) Dot plot showing the scaled expression and fraction of cells expressing marker genes for each cell phenotype. **C**) UMAP of myeloid cells, colored by cell phenotype. **D**) Dot plot showing the scaled expression and fraction of cells expressing marker genes associated with each myeloid cell phenotype. **E**) UMAP of B cells, with likely-healthy and likely-malignant cells distinguished. **F**) Frequency of likely-healthy and likely-malignant B cells in samples with each diagnosis. **G**) Dot plot showing the scaled expression and fraction of cells expressing each costimulatory receptor. **H**) Volcano plot of genes differentially expressed between DCs and B cells. P-values are calculated with a two-sided Wilcoxon rank-sum test and are adjusted using Bonferroni correction.

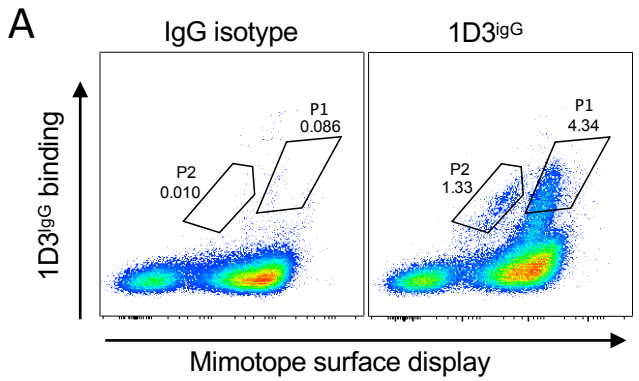

B

Top-ranked 1D3 mimotopes

H1 SKLKGKSGPE
C11 FHWFINVPPF
E2 IRVLMSRVFA

Mimotopes	Sequence
H1	SKLKGKSGPE
H1C11	SKLKGKSGPEFHWFINVPPF
H1E2	SKLKGKSGPEIRVLMSRVFA

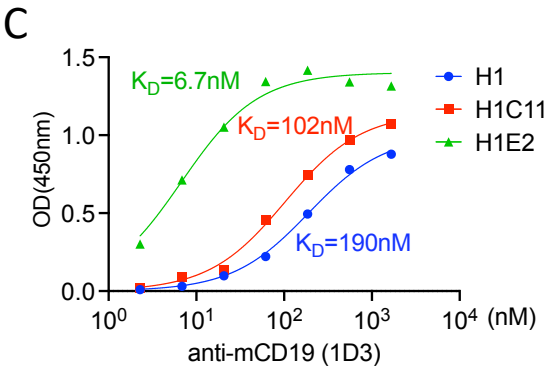

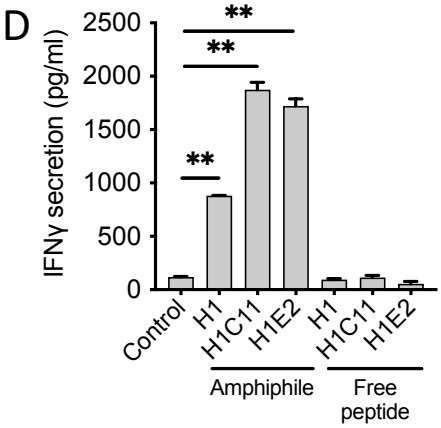

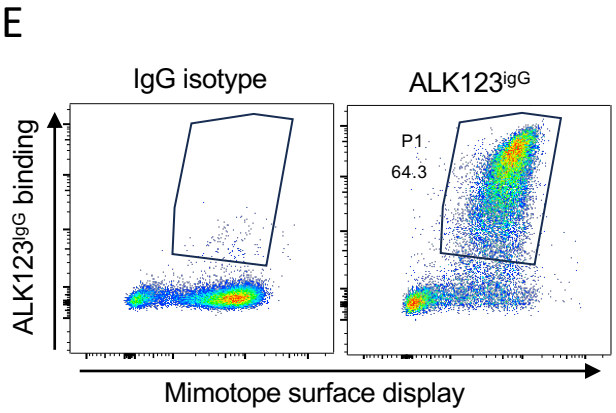

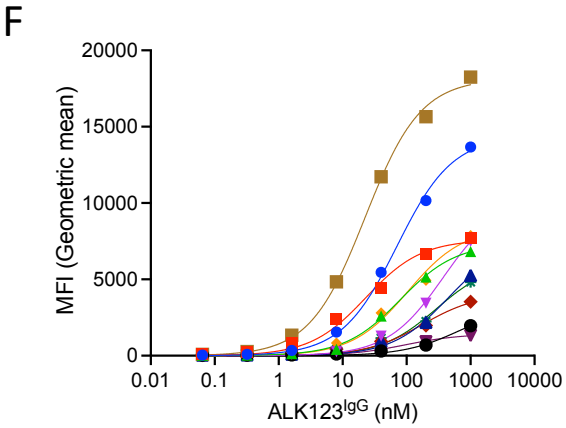

	Mimotope sequence	Kd (nM)
A2	LLLSWDPWRIECLPP	70.77
A3	TEAEGRLAWCRKWAYV	23.01
A6	RMDSRFMVDWPCLNW	79.85
A11	SYDFQCFPWCGH	373.9
C1	GWNPWADIACSLP	103.7
C5	ACSSFKTWPCWPE	657.7
E4	SPWWDNDPPP	22.48
F5	SSLSGPCKYCWYK	440.7
F6	PRLSLCTIVLDCRGL	95.96
G6	SMQLMRSDYGCPPR	174.9
H4	YPKLRCVEWT	293.6

509

Extended Data Figure 4. Identification of mimotopes specific for anti-mouse CD19 and anti-ALK antibodies. (**A-D**) Identification of a mimotope for anti-mouse CD19 mAb 1D3. (**A**) Flow cytometry scatter plots illustrating successful identification of yeast cells binding to $1D3_{IgG}$ at 1μM. Two yeast populations, P1 and P2, were identified. (**B**) Top-ranked 1D3 mimotopes. Shown in the table are individual mimotopes and mimotope fusions. (**C**) ELISA showing the binding of $1D3_{IgG}$ to chemically synthesized mimotopes in B. A one site-specific binding model was used for assessing the apparent binding affinity (Kd). (**D**) Mouse IFN-γ secretion from anti-mouse CD19 CAR T cells co-cultured with target cells labeled with 100nM of amph-mimotopes or free mimotope peptides. Error bars show mean ± s.d. with three replicates. **, $p<0.01$ by one-way ANOVA with Turkey's post-test. (**E-F**) Identification of a mimotope for ALK-specific mAb ALK123. (**E**) Flow cytometry plots showing the successful identification of yeast cells binding to $ALK123_{IgG}$ at 500nM. (**F**) Binding of $ALK123_{IgG}$ to select yeast clones. Amino acid sequences were shown for each yeast clone. A one site-specific binding model was used for assessing the apparent binding affinity (Kd).

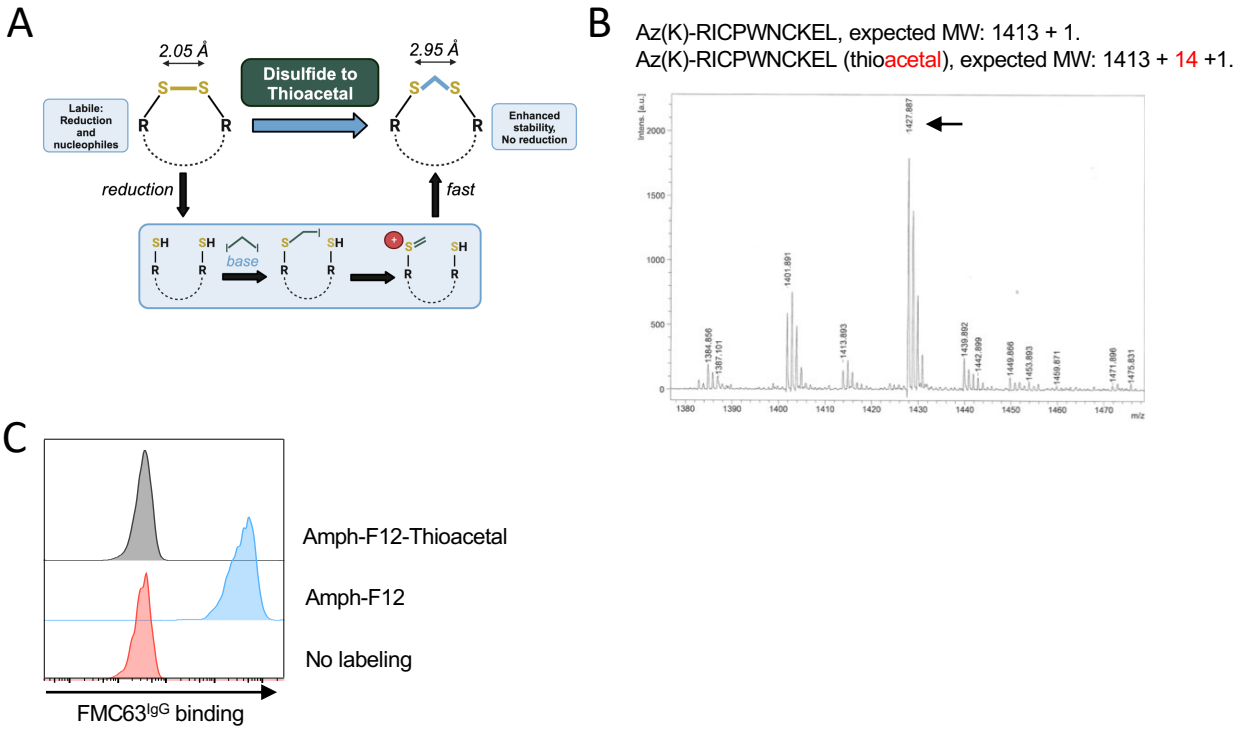

Extended Data Figure 5. Converting the disulfide bond to a thioacetal bond prevents mimotope binding to FMC63^{IgG}. (**A**) schematics showing the chemical structure and conversion of the disulfide bond to a thioacetal bond. (**B**) MALDI spectrum showing the purification of expected mimotope with a thioacetal bond. (**C**) Representative histogram showing FMC63^{IgG} binding to target cells labeled with amph-mimotope^{F12} variants.

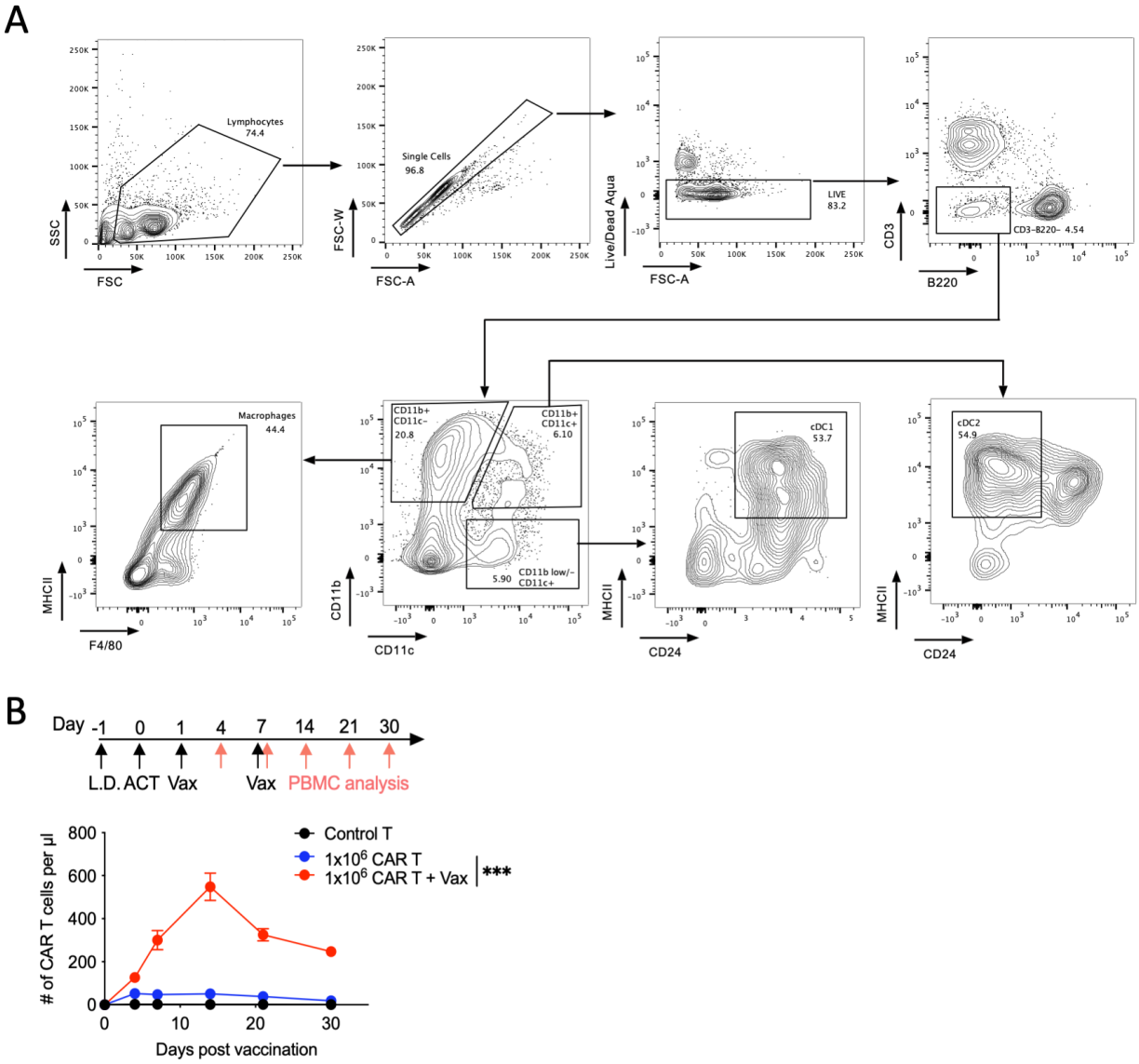

Extended Data Figure 6. Amph-mimotope labeling of APCs and stimulation of FMC63-mCAR T cell expansion *in vivo*. (**A**) Gating strategies and surface makers used for defining APC populations in the lymph node. (**B**) C57BL/6 mice (*n*=5 animals/group) were lymphodepleted (L.D.) with 500cGy gamma irradiation, adoptively transferred with 10^6 FMC63 CAR-T cells, and then vaccinated at indicated time points. Shown are the number of circulating FMC63-mCAR-T cells per microliter of blood quantified by flow cytometry over time. This data is related to Fig 5E. Error bars show mean ± 95% CI. ***, p<0.0001 by two-way ANOVA with Tukey's post-test.

606 **References**

607 1. Maude, S. L. *et al.* Chimeric antigen receptor T cells for sustained remissions in leukemia.
608 *New Engl J Medicine* **371**, 1507–17 (2014).

609 2. Kadauke, S. *et al.* Risk-Adapted Preemptive Tocilizumab to Prevent Severe Cytokine
610 Release Syndrome After CTL019 for Pediatric B-Cell Acute Lymphoblastic Leukemia: A
611 Prospective Clinical Trial. *J Clin Oncol* JCO.20.02477 (2021) doi:10.1200/jco.20.02477.

612 3. Frey, N. V. *et al.* Optimizing Chimeric Antigen Receptor T-Cell Therapy for Adults With Acute
613 Lymphoblastic Leukemia. *J. Clin. Oncol. : Off. J. Am. Soc. Clin. Oncol.* **38**, 415–422 (2019).

614 4. Maude, S. L. *et al.* Chimeric Antigen Receptor T Cells for Sustained Remissions in Leukemia.
615 *New England Journal of Medicine* **371**, 1507–1517 (2014).

616 5. Deventer, J. A. V. & Wittrup, K. D. Monoclonal Antibodies, Methods and Protocols. *Methods*
617 *Mol. Biol.* **1131**, 151–181 (2014).

618 6. Angelini, A. *et al.* Protein Engineering and Selection Using Yeast Surface Display. *Methods*
619 *Mol. Biol. (Clifton, NJ)* **1319**, 3–36 (2015).

620 7. Ma, L. *et al.* Enhanced CAR–T cell activity against solid tumors by vaccine boosting through
621 the chimeric receptor. *Science* **365**, 162–168 (2019).

622 8. Ma, L. *et al.* A therapeutically targetable mechanism of BCR-ABL-independent imatinib
623 resistance in chronic myeloid leukemia. *Science translational medicine* **6**, 252ra121-252ra121
624 (2014).

625 9. Kourra, C. M. B. K. & Cramer, N. Converting disulfide bridges in native peptides to stable
626 methylene thioacetals. *Chem. Sci.* **7**, 7007–7012 (2016).

627 10. Ma, L. *et al.* Vaccine-boosted CAR T crosstalk with host immunity to reject tumors with
628 antigen heterogeneity. *Cell* **186**, 3148-3165.e20 (2023).

629 11. Jumper, J. *et al.* Highly accurate protein structure prediction with AlphaFold. *Nature* **596**,
630 583–589 (2021).

631 12. Rohl, C. A., Strauss, C. E. M., Misura, K. M. S. & Baker, D. Protein Structure Prediction
632 Using Rosetta. *Methods Enzym.* **383**, 66–93 (2004).

633 13. Park, H. *et al.* Simultaneous Optimization of Biomolecular Energy Functions on Features
634 from Small Molecules and Macromolecules. *J. Chem. Theory Comput.* **12**, 6201–6212 (2016).

635 14. Alford, R. F. *et al.* The Rosetta All-Atom Energy Function for Macromolecular Modeling and
636 Design. *J. Chem. Theory Comput.* **13**, 3031–3048 (2017).

637 15. Nivón, L. G., Moretti, R. & Baker, D. A Pareto-Optimal Refinement Method for Protein
638 Design Scaffolds. *PLoS ONE* **8**, e59004 (2013).

639 16. Krissinel, E. & Henrick, K. Inference of Macromolecular Assemblies from Crystalline State.
640 *J. Mol. Biol.* **372**, 774–797 (2007).

641 17. Nair, S., Archer, G. E. & Tedder, T. F. Isolation and Generation of Human Dendritic Cells.
642 *Curr. Protoc. Immunol.* **99**, 7.32.1-7.32.23 (2012).

643 18. Han, T. H. *et al.* Evaluation of 3 clinical dendritic cell maturation protocols containing
644 lipopolysaccharide and interferon-gamma. *J. Immunother. (Hagerstown, Md : 1997)* **32**, 399–
645 407 (2009).

646 19. Witkowski, M. T. *et al.* Extensive Remodeling of the Immune Microenvironment in B Cell
647 Acute Lymphoblastic Leukemia. *Cancer Cell* **37**, 867-882.e12 (2020).

648 20. Charan, J. & Kantharia, N. D. How to calculate sample size in animal studies? *J Pharmacol*
649 *Pharmacother* **4**, 303–306 (2013).

650 21. Moynihan, K. D. *et al.* Eradication of large established tumors in mice by combination
651 immunotherapy that engages innate and adaptive immune responses. *Nature Medicine* **22**,
652 1402–1410 (2016).

653 22. Davila, M. L., Kloss, C. C., Gunset, G. & Sadelain, M. CD19 CAR-Targeted T Cells Induce
654 Long-Term Remission and B Cell Aplasia in an Immunocompetent Mouse Model of B Cell Acute
655 Lymphoblastic Leukemia. *PLOS ONE* **8**, e61338-14 (2013).

656 23. Adachi, K. *et al.* IL-7 and CCL19 expression in CAR-T cells improves immune cell infiltration
657 and CAR-T cell survival in the tumor. *Nature Biotechnology* **36**, 346–351 (2018).

658